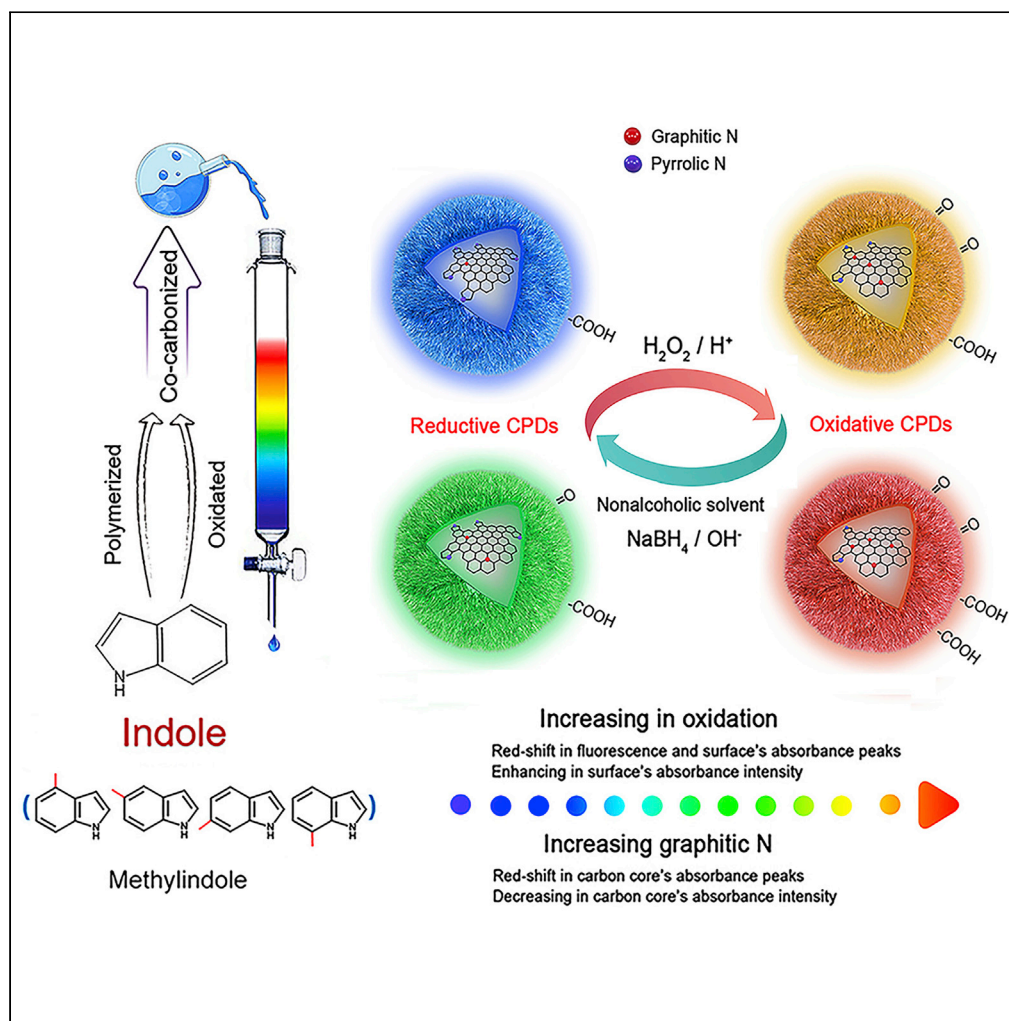## Article

Indole Carbonized Polymer Dots Boost Full-Color Emission by Regulating Surface State

Chang Liu, Yanzi Jin, Ruijie Wang, ..., Chengzhi Huang, Shoujun Zhu, Jiucun Chen

chengzhi@swu.edu.cn (C.H.)
sjzhu@jlu.edu.cn (S.Z.)
chenjc@swu.edu.cn (J.C.)

HIGHLIGHTS

Achieving a palette of full-color light-emissive CPDs in a single reaction system

Providing the surface-state engineering rules for CPDs' emission centers

Enriching the guidance library for studying the fluorescence mechanism of CPDs

Article

Indole Carbonized Polymer Dots Boost Full-Color Emission by Regulating Surface State

Chang Liu,[1] Yanzi Jin,[1] Ruijie Wang,[1] Tianyang Han,[2] Xiangping Liu,[2] Bing Wang,[1] Chengzhi Huang,[3,*] Shoujun Zhu,[2,4,*] and Jiucun Chen[1,5,*]

SUMMARY

Carbonized polymer dots (CPDs) are impressive imaging probes with great potential for enriching the library of metal-free fluorescent materials, yet current strategies have struggled to achieve products that emit full-color light in a single reaction system. Establishing an efficient and robust synthesis approach that unlocks the color barrier to the luminescence centers of specific CPDs remains a challenge. Herein, the surface-state engineering of pyridine and amide in the indole system to create a palette of resolvable full-color light-emissive CPDs is reported. Detailed structural analysis revealed that cationic polymerization and oxidation reactions potentially contribute to the formation of the main frameworks and emission centers of the final CPDs, with emissive oxygen- and nitrogen-based centers fixed by cross-linked polymer structures. This study provides valuable insight into the energy absorbance and photoluminescence mechanism of CPDs and introduces additional reactants (benzo heterocycle) into CPD research.

INTRODUCTION

Fluorescence probes have ushered in a new era of material selection, as carbon dots (CDs) afford metal-free contrast agents for use in biological visualization and biosensor fields (Tao et al., 2012; Liu et al., 2015b, 2015c; Li et al., 2018a; Kong et al., 2016; Xiong et al., 2018; Yuan et al., 2016; Qu et al., 2012; Jiang et al., 2018). Many academic publications have repeatedly revealed that CDs can serve as efficient fluorophores in several color regions (Nie et al., 2014; Ge et al., 2015; Li et al., 2018b). However, current CDs suffer from unresolved issues in terms of unclear structures and photoluminescence (PL) mechanisms (Zhu et al., 2015). Improving multi-channel CDs is critical for visualizing multiple biological processes and other related applications (Kim et al., 2017; Jiang et al., 2015; Kong et al., 2012; Hola et al., 2014). Besides, the structural details of each single reaction system need to be elucidated to accurately determine the CD PL mechanism.

Carbonized polymer dots (CPDs) from specific polymerization and carbonization systems provide the impetus for overcoming the current challenges in CD research, as CPDs are mainly formed by polycondensing monomers before further carbonization. The chemical structures of CPDs are relatively clear, which avoids complicating factors associated with the traditional CD system, and the derived PL mechanism convincingly involves single emission centers (Xia et al., 2019; Tao et al., 2019). A comprehensive principle for achieving a palette of full-color light-emissive CPDs in a single reaction system that fully addresses the PL emission centers is still lacking.

Full-color light-emissive CPDs have the potential to fundamentally alter current CD research, providing efficient synthesis and purification strategies for long-wavelength and/or near-infrared-emissive metal-free fluorophores (Gao et al., 2018a). Notably, the resolvable spectral domain will add sufficient multiplex channels that target a number of distinct species, particularly when visualizing complicated biological events (Deng et al., 2019; Pansare et al., 2012; Gao et al., 2018b). Hence, there is an urgent need to prepare and exploit CPDs with tunable emission wavelengths in the broad visible to the red region. Exploiting the PL mechanism and elucidating the relationship between chemical structure and PL emission centers is also highly desirable in the field of CPDs and other CD-derived materials.

[1]Chongqing Key Laboratory for Advanced Material & Technologies of Clean Energies, School of Materials and Energy, Southwest University, Chongqing 400715, P. R. China

[2]State Key Laboratory of Supramolecular Structure and Materials, College of Chemistry, Jilin University, Changchun 130012, P. R. China

[3]College of Pharmaceutical Sciences, Southwest University, Chongqing 400715, P. R. China

[4]Key Laboratory of Organ Regeneration & Transplantation of the Ministry of Education, The First Hospital of Jilin University, Changchun 130061, P. R. China

[5]Lead Contact

*Correspondence:
chengzhi@swu.edu.cn (C.H.),
sjzhu@jlu.edu.cn (S.Z.),
chenjc@swu.edu.cn (J.C.)
https://doi.org/10.1016/j.isci.2020.101546

To address these issues, an efficient synthesis route to a palette of full-color light-emissive CPDs that uses a single indole system was developed. Sets of full-color emissive centers are generated by solvothermally treating indole under acidic and oxidizing conditions that serve to cationically polymerize and oxidize it. The mixed emissive centers (oxygen- and nitrogen-based groups) were confirmed by a series of characterization techniques and purified by column chromatography to afford single-peak-emissive CPDs. The emission center is closely related to the chemical structure of the CPD; higher percentages of O/N groups in the separated CPDs potentially result in longer emission wavelengths. To provide strong evidence for the surface-state mechanism operating in these CPDs, further well-designed experiments that investigated the effects of solvent, acidity, and redox conditions were performed.

RESULTS

Synthesis of Indole CPDs and Their Formation Mechanism

Multiple color-emissive CPDs were constructed through the solvothermal treatment of indole in ethanol in the presence of acid (HCl) and an oxidizer (H_2O_2) (Figure 1A). The crude product was a dark multi-component red-brown liquid that was effectively separated by silica-gel column chromatography. Figure 1B displays a photographic image that shows the component distribution in the silica-gel column when excited by 365-nm UV light, which reveals that longer fluorescence wavelengths correspond to higher CPD polarity. It is worth noting that the regular distribution of CPDs is conducive to precise separation and purification. Ten pure CPDs were obtained after removing the redundant solvent by reduced-pressure distillation, with their ethanol solutions fluorescing with colors that ranged from violet to orange-red when UV irradiated, as depicted in Figure 1C. For convenience, these CPDs are, respectively, labeled "CPDs-1," "CPDs-2," to "CPDs-10" with increasing fluorescence redshift. To determine the most appropriate conditions for the synthesis of a product with a high proportion of components that fluoresce at long wavelengths, the key reaction conditions were first optimized, including the reaction temperature, time, and the HCl and H_2O_2 dosages (Figures S1 and S2). This process not only helped select the optimal reaction conditions but also revealed that both HCl and H_2O_2 are essential for the CPD formation. In addition, the CPD yields at various dosages of H_2O_2 and HCl (Tables S1 and S2) revealed that the use of the appropriate amount of H_2O_2 increased the amount of product with long-wavelength emissions (CPDs-7 to CPDs-10), suggesting that the oxidizer was mostly responsible for producing long-wavelength emissions. Additionally, HCl can be also replaced with an equivalent strong acid, such as H_2SO_4, H_3PO_4, and CF_3COOH, but it cannot be replaced with an oxidizing acid (that is, HNO_3) or a weak acid (that is, CH_3COOH). Similarly, H_2O_2 can be replaced with periodic acid and *tert*-butylperoxide, as both reagents also produce O_2 through pyrolysis (Figure S3) (the speculations were provided in Supplemental Information). With these results in mind, typical optimal reaction conditions included placing a raw material solution composed of 0.7 mM HCl, 1.6 mM H_2O_2, 3.4 mM indole, and 10.0 mL ethanol in a 20.0-mL Teflon-lined stainless-steel autoclave and heating at 180°C for 1.5 h.

How HCl and H_2O_2 participate in the formation of CPDs was investigated next. Indoline and seven isomeric methylindoles were treated under the above-mentioned optimal conditions and then subjected to silica-gel column chromatography. As depicted in Figure 1D, multicolor luminescence was observed for the indoles substituted with methyl groups on their benzene rings, indicating that the benzene ring had little overall effect on the reaction. In sharp contrast, indoline, 2-methylindole, and 3-methylindole failed to produce a full-color mixture; however, 1-methyl indole did. Even with multicolor luminescence observed in the silica-gel column, the 1-methylindole-derived CPDs were significantly less bright, especially in the long-wavelength region. When the results for indoline and indole are compared, it was clear that the unsaturated C=C bond of the pyrrole ring plays a dominant role in CPD formation. In the case of 2-methylindole and 3-methylindole, steric hindrance arising from the methyl group may hinder the reaction of the pyrrole C=C bond and any derivatives. In the case of 1-methylindole, the methyl group on the nitrogen impedes the protonation of the pyrrole ring under acidic conditions (Sun and Shi, 2014).

Indole is well known to be a significant monomer in the manufacture of conducting polymers; polyindole is produced by electropolymerization, chemical oxidation, or cationic polymerization (Phasuksom and Sirivat, 2016; Koiry et al., 2007; Tiwari et al., 2015). Before solvothermal treatment, the addition of HCl and H_2O_2 to the ethanolic indole precursor solution was expected to induce polymerization at ambient pressure and temperature (Figure S4), the precursor solution quickly turned blackish-green and was accompanied by the gradual appearance of visible precipitates at a specific dosage of H_2O_2. Overall, H_2O_2 not only plays
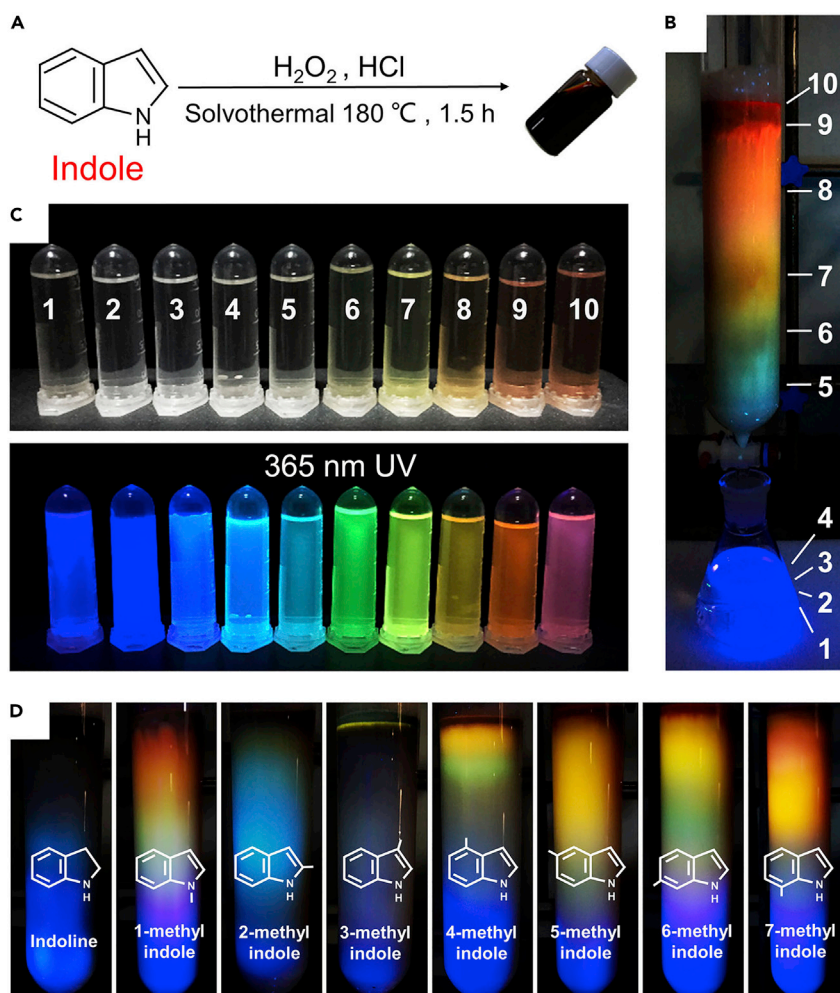
Figure 1. One-Pot Synthesis and Purification of Indole-Based CPDs with Full-Color Emission

(A) Synthesis of CPDs by the solvothermal treatment of indole in acidic ethanol containing H_2O_2.

(B) Photographic image of distinct CPD components on a silica-gel column when irradiated with 365-nm UV light (eluent: ethyl acetate/ethanol).

(C) Photographic image of the 10 CPD samples under white light and 365-nm UV light.

(D) Photographic images of the distinct products synthesized from indoline and seven isomeric methylindoles on silica-gel columns when irradiated with 365-nm UV light.

See also Tables S1 and S2 and Figures S1–S4.

a role in the polymerization of indole in an acidic solution but also serves as an oxidizer for the generation of oxidized polyindole or oxoindole. However, compared with the solvothermally produced products, the above-mentioned polymerized products lacked notable fluorescence properties.

Taken together, the study confirmed a synchronous reaction process involving acid-promoted cationic polymerization, oxidation, and solvothermal carbonization, as expected, during the formation of these CPDs (Soylu et al., 2011; Siddiquee and de Klerk, 2015, Speicher et al., 2012). As depicted in Figure 2A, the initial step involved protonation to form the indolium ion, followed by the formation of oligomers or polyindole. Meanwhile, the C=C bond of the pyrrole ring can also be attacked by O_2 to generate a hydroperoxide, and this active intermediate further reacts to produce oxidized polyindole or oxoindole (Figure 2B). At a certain polyindole/oxoindole ratio, imbalanced carbonization during the solvothermal process produces CPDs with various emission centers and polarities (Figure 2C), which can be further separated and purified by silica-gel chromatography.
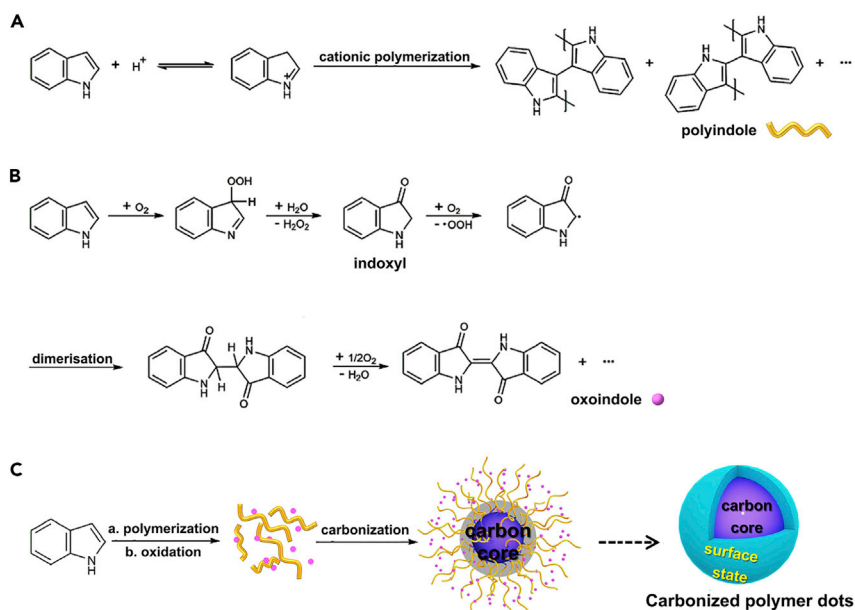
A

B

C

Figure 2. Depicting the Formation of CPDs

(A) Acid-promoted cationic polymerization of indole.

(B) Unbalanced oxidation of indole.

(C) Schematic diagram depicting the mechanism for the formation of CPDs. Polyindole and oxoindole were further carbonized to form CPDs.

See also Figures S5 and S6.

The CPDs were characterized and their chemical structures quantified using typical techniques. The Fourier transform infrared (FTIR) spectrum of indole (Figure S5) reveals peaks at 3,422 and 1,561 cm^{-1} that correspond to stretching and deformation vibrations of the N−H bond of the pyrrole ring, respectively. The C−H bonds of the aromatic ring (that is, Ar−H) stretch and bend in an out-of-plane manner, resulting in peaks at 3,050 and 741 cm^{-1}, respectively. The small peak at 720 cm^{-1} is ascribable to the in-phase vibrations of the C−H bonds at the 2- and 3-positions of the pyrrole ring (Speicher et al., 2012). By comparison, the characteristic N−H and Ar−H peaks are still observable in the spectra of the CPDs, meaning that the benzene ring and nitrogen atom are not the main reaction sites. The disappearance of the peak at 720 cm^{-1} reveals that the 2- and 3-positions of indole are involved in polymerization (Phasuksom and Sirivat, 2016; Koiry et al., 2007; Tiwari et al., 2015). A new peak at 1,700 cm^{-1} is observed, consistent with the formation of a C=O bond, which confirms that oxidation has occurred. The subsequent solvothermal reaction promotes cross-linking and the partial carbonization of indole, polyindole, and oxidized polyindole, which are reflected through the broadening of the N−H band (3,430 cm^{-1}), weakening of the Ar−H bands (3,061 and 740 cm^{-1}), and enhanced aliphatic C−H bands (2,850–2,920 cm^{-1}).

Moreover, ^{1}H and ^{13}C nuclear magnetic resonance (NMR) spectroscopies were employed to determine the chemical constitution of the CPDs. The ^{1}H NMR spectrum of indole (Figure S6A) exhibits only signals between 6.56 and 8.15 ppm that correspond to a conjugated system, whereas the spectra of the CPDs show more peaks, especially at lower chemical shifts (0.87–5.34 ppm), that are attributed to sp^3-hybridized carbons, amines, or H−C−O/N units (Zhu et al., 2013; Li et al., 2017). The peaks in the 6.46–8.08 ppm range in the CPD spectra originated from protons in the N-doped carbon cores (Zhao et al., 2017), whereas the peak at 8.08 ppm is ascribable to a pyrrole-ring proton because it is similar to the analogous peak in the spectrum of indole. Furthermore, the peaks at 8.79 and 9.05 ppm, which are assigned to H−C=O units, are consistent with oxidation of the heterocyclic surface of the CPD (Wang et al., 2011). Similarly, the CPDs show more peaks than indole in their ^{13}C NMR spectra (Figure S6B), including new signals associated with carbonyl groups in the 167–173 ppm range and sp^3-hybridized carbon atoms (for example, C−C, C−N, and C−O) at 13–36 ppm. The signals in the 99–150 ppm range correspond to conjugated carbon atoms, namely, sp^2 carbons, which mainly exist on the graphitized core or in C=N structures (Yang et al., 2015, 2019).
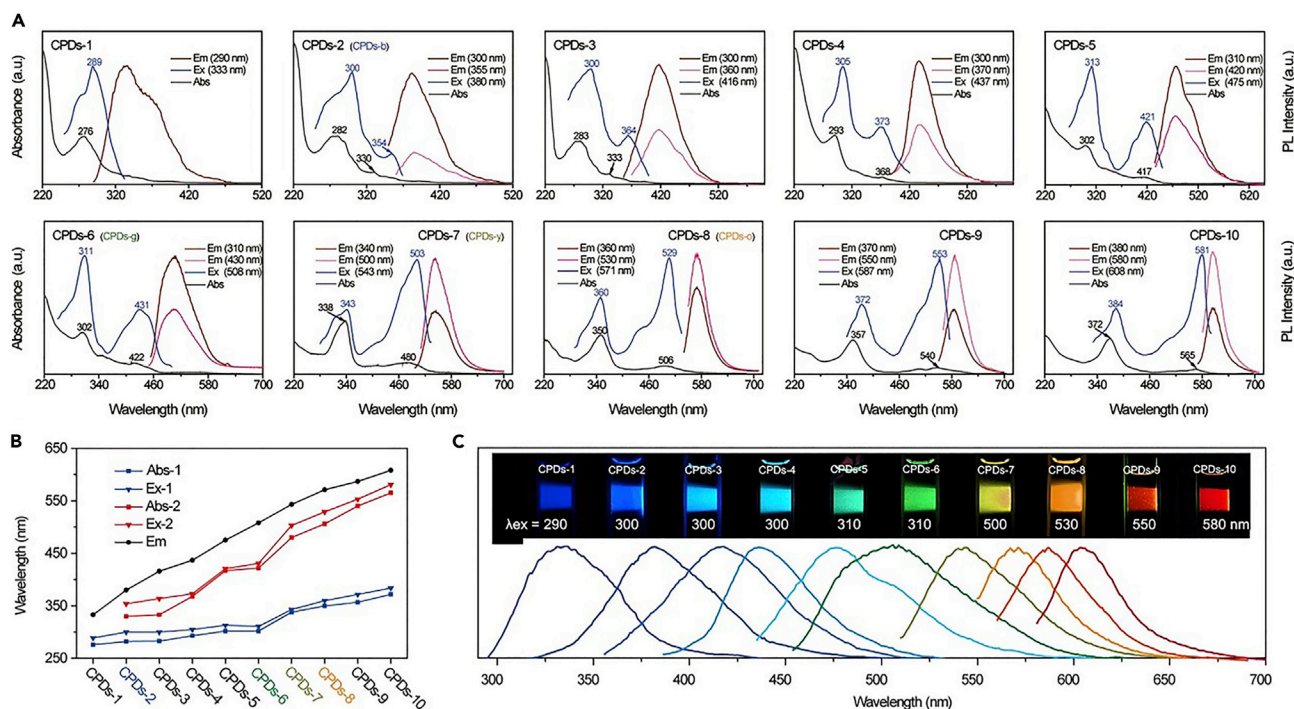
Figure 3. Characterizing the Optical Properties of the 10 CPD Samples

(A) UV-visible absorption (black), PL excitation (Ex) (red and pink), and emission (Em) (blue) spectra of the CPD solutions.

(B) Dependence of the wavelengths of the first and second absorption peaks (Abs-1 and Abs-2), first and second excitation peaks (Ex-1 and Ex-2), and emission peaks (Em) on the CPD (the data are presented in Table S3).

(C) Photographic images and corresponding emission spectra of the 10 samples, with optimal emissions at 333, 380, 416, 437, 475, 508, 543, 571, 587, and 608 nm.

See also Table S3 and Figure S7.

Optical Properties and Full-Color Emission of CPDs

Except for CPDs-1, the UV-visible absorption (Abs) spectra of the prepared CPDs display two obvious absorption peaks, as depicted in Figure 3A (black spectra). Similar absorption peaks, with redshifts in the longer wavelength region (that is, the second peak at 330–565 nm, referred to as "Abs-2," which is ascribed to n-π* transitions of C=O/C=N groups) are observed in moving from CPDs-2 to CPDs-10. Similarly, in the UV region (283–372 nm), the wavelength of the first absorption peak (Abs-1) gradually redshifts in moving from CPDs-1 to CPDs-10. Abs-1 peaks are considered to correspond to π-π* transitions in the aromatic rings on the core (Wu et al., 2017a; Zheng et al., 2014). Furthermore, the PL excitation (Ex) spectra (Figure 3A, blue spectra) show two peaks (Ex-1 and Ex-2) with positions quite close to the corresponding absorption peaks, indicating the clear energy absorbance centers in terms of carbon core and surface states. More interestingly, the Stokes shift in some CPDs exceeded 200 nm (Table S3), which is beneficial for nonoverlapping emission channels and enhances specificity during bioimaging (Wu et al., 2017b). A positive correlation was also observed between the emission (Em) wavelength and the CPD, Abs-1 and Ex-1, as well as Abs-2 and Ex-2 (Figure 3B and Table S3); CPDs-1 to CPDs-10 emitted at 333, 380, 416, 437, 475, 508, 543, 571, 587, and 608 nm, respectively, with an average deviation of ~8 nm. The CPD fluorescence emission range covered the full-color region, from UV to red, consistent with the color distribution observed in the original silica-gel column. Figure 3C depicts photographic images of the fluorescence of each CPD and the corresponding emission spectrum acquired at the corresponding optimal excitation wavelength. Their Commission International de I' Eclairage (CIE) color coordinate changed from [0.1698, 0.0067] to [0.6320, 0.3676], covering the warm and cold color series (see Figure S7).In addition, the study also found that the contribution of surface states increased in moving from CPDs-1 to CPDs-10. As depicted in Figure 3A, CPDs-2 to CPDs-6 exhibit peak intensities such that Ex-1 > Ex-2 and Em-1 > Em-2 (Em-1 and Em-2 are emission peaks with shorter and longer excitation wavelengths, respectively). In contrast, Ex-1 < Ex-2 and Em-1 < Em-2 were observed for

CPDs-7 to CPDs-10, which implies a weakening dependence of the long-wavelength emission from the carbon core.

To further investigate the optical properties and the PL mechanism, CPDs-2, CPDs-6, CPDs-7, and CPDs-8 were selected and renamed according to their emission colors as "CPDs-b," "CPDs-g," "CPDs-y," and "CPDs-o," respectively, because they emitted bright blue, green, yellow, and orange luminescence in ethanol when irradiated with UV light (Figure 4A). The spectra in Figure 4B reveal that the Abs-1 wavelengths of CPDs-b, CPDs-g, CPDs-y, and CPDs-o are 282, 302, 338, and 350 nm, respectively, with corresponding Abs-2 values of 330, 422, 480, 506 nm, respectively; the absorption-wavelength edges were determined to be 409, 473, 536, and 586 nm, respectively. According to the well-established formula (Yuan et al., 2018) of $E_g = 1,240/\lambda_{abs}$ (E_g, optical band gap energy; λ_{abs}, absorption-edge wavelength), the optical band gap energy (E_g) of CPDs-b, CPDs-g, CPDs-y, and CPDs-o were determined to be 3.0, 2.6, 2.3, and 2.1 eV, respectively. As depicted in Figure 4C, CPDs-b, CPDs-g, CPDs-y, and CPDs-o displayed individual optimal PL emissions (380, 508, 543, and 571 nm, respectively) when irradiated at their corresponding excitation wavelengths (300, 310, 500, and 530 nm, respectively). All CPDs exhibited excitation-independent emissions, which indicate the existence of a single, pure luminescence center in each CPD (Dong et al., 2013; Yeh et al., 2016; Yang et al., 2016). The existence of simple emission centers with single radiation processes was further confirmed by time-resolved photoluminescence (TRPL) spectroscopy, as depicted in Figure S8. The PL decay of each CPD was monoexponential, with a lifetime that is independent of Ex-1 or Ex-2 excitation (Liu et al., 2018). Moreover, the PL lifetime showed a notable decreasing trend in moving from CPDs-b to CPDs-g, CPDs-y, and CPDs-o (12.4–8.1, 6.9, and 2.1 ns), which is ascribable to somewhat slower carbon-core to surface carrier relaxation when excited at shorter wavelengths, whereas direct carrier recombination is faster on the surface when excited at longer wavelengths (Han et al., 2017).

The absolute photoluminescence quantum yields were also determined when excited at both Ex-1 and Ex-2, with values of 26% (λ_{ex} = 300 nm, Ex-1) and 21% (355 nm, Ex-2) obtained for CPDs-b, 22% (310 nm) and 18% (430 nm) for CPDs-g, 15% (340 nm) and 12% (500 nm) for CPDs-y, and 10% (360 nm) and 7% (530 nm) for CPDs-o (in ethanol). The observed variations were due to bigger Stokes shifts resulting in weaker self-absorption and less lost energy (Wu et al., 2017b). Taken together, it was concluded that the oxygen-based groups of the surface states contribute to PL centers, and that CPDs with specific surface states can be completely separated on the basis of polarity (Ding et al., 2016; Bao et al., 2011).

Structures and Chemical Compositions of CPDs-b, CPDs-g, CPDs-y, and CPDs-o

The transmission electron microscopic (TEM) images displayed in Figure 5A revealed that CPDs-b, CPDs-g, CPDs-y, and CPDs-o are composed of particles of very similar size, with average sizes of 2.6, 2.8, 2.9, and 3.3 nm, respectively. The high-resolution TEM images (Figure 5A) show that these samples contained partially ordered internal structures. Two lattice fringes, with a spacing of 0.23 and 0.36 nm, were observed (Sun et al., 2015, 2016; Miao et al., 2018); the 0.36 nm spacing is larger than the theoretical interlayer spacing (0.34 nm) of graphite. Enlargement of the interlayer distance is attributable to heteroatom doping in the core and increasing numbers of functional groups at the edge. Atomic force microscopy further confirmed that the CPDs are monodispersed and quasi-spherical nanoparticles. As depicted in Figure 5B, the average heights of CPDs-b, CPDs-g, CPDs-y, and CPDs-o were 2.6 nm (1.4–4.0 nm), 2.2 nm (1.4–3.0 nm), 3.2 nm (1.4–4.6 nm), and 3.1 nm (1.6–5.7 nm), respectively.

The X-ray diffraction (XRD) pattern of each of the four CPDs (Figure 5C) exhibits an obvious broad peak centered at 21°, and two micro peaks at ~26.4° and 45.1°. The broad peak corresponds to amorphous carbon that originates from deformations caused by the heteroatomic dopants or sp^3 C defects in graphitic structures. According to the Joint Committee on Powder Diffraction Standards (JCPDS) card (graphite 2H: PDF#75-1621), the minor peak at 26.4° corresponds to the (002) facet with an interlayer spacing of 0.34 nm, whereas the peak at 45.1° is due to the (101) facet with an interlayer spacing of 0.20 nm. The XRD data revealed that these CPDs appeared to possess a more amorphous structure.

Figure 5D reveals that the Raman spectrum of each CPD exhibits two peaks, at approximately 1,360 and 1,585 cm^{-1}, and that these peaks correspond to D- and G-bands that are related to disordered and graphitic structures, respectively (Wang et al., 2017). Additionally, the I_D/I_G ratios can be used to determine
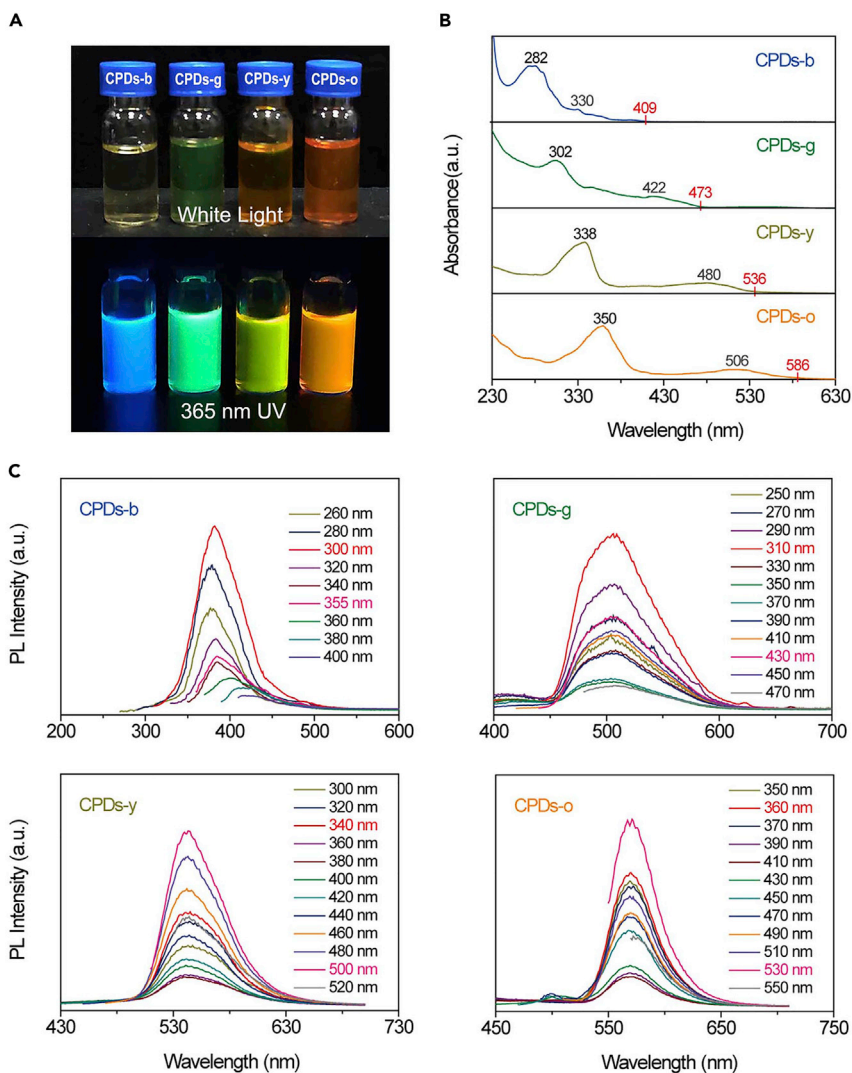
Figure 4. Four Typical CPDs, Namely, CPDs-b, CPDs-g, CPDs-y, and CPDs-o, Were Selected for Further Investigation
(A) Photographic images of ethanol solutions of the four CPDs when excited with white and 365-nm UV light.
(B) Normalized UV-visible absorption spectra of the CPD solutions.
(C) PL emission spectra of the CPD solutions when excited at different wavelengths.
See also Table S3 and Figure S8.

the proportion of defect parts (sp^3 components), which were calculated to be 0.89, 0.95, 1.01, and 1.06 for CPDs-b, CPDs-g, CPDs-y, and CPDs-o, respectively. The increasing I_D/I_G trend indicated that the PL redshift observed for these CPDs is associated with a decrease in the degree of graphitization and an increase in the proportion of oxygen/nitrogen-based groups (emission centers).

The FTIR spectra (Figure 5E) revealed N−H/O−H (peak centered at 3,402 cm^{-1}), aliphatic C−H (2,964–2,840 cm^{-1}), C=O (1,723 cm^{-1}), C=N (1,608 cm^{-1}), C=C (1,537 cm^{-1}), and C−N= (1,450 cm^{-1}) stretching vibrations that confirmed the existence of polyaromatic structures connected to O- and N-containing functional groups. In addition, some unusual trends were observed for the four CPDs. (1) The characteristic C=O peaks increased in intensity in moving from CPDs-b, to CPDs-g, CPDs-y, and CPDs-o, which clearly indicates an increasing oxidation trend, that is, the PL redshift is associated with an enhanced degree of oxidation (Bao et al., 2011). (2) The peak at around 3,402 cm^{-1} is discrete and sharp in the spectra of CPDs-b and CPDs-g, but continuous and broad for CPDs-y and CPDs-o, which reflects the fact that
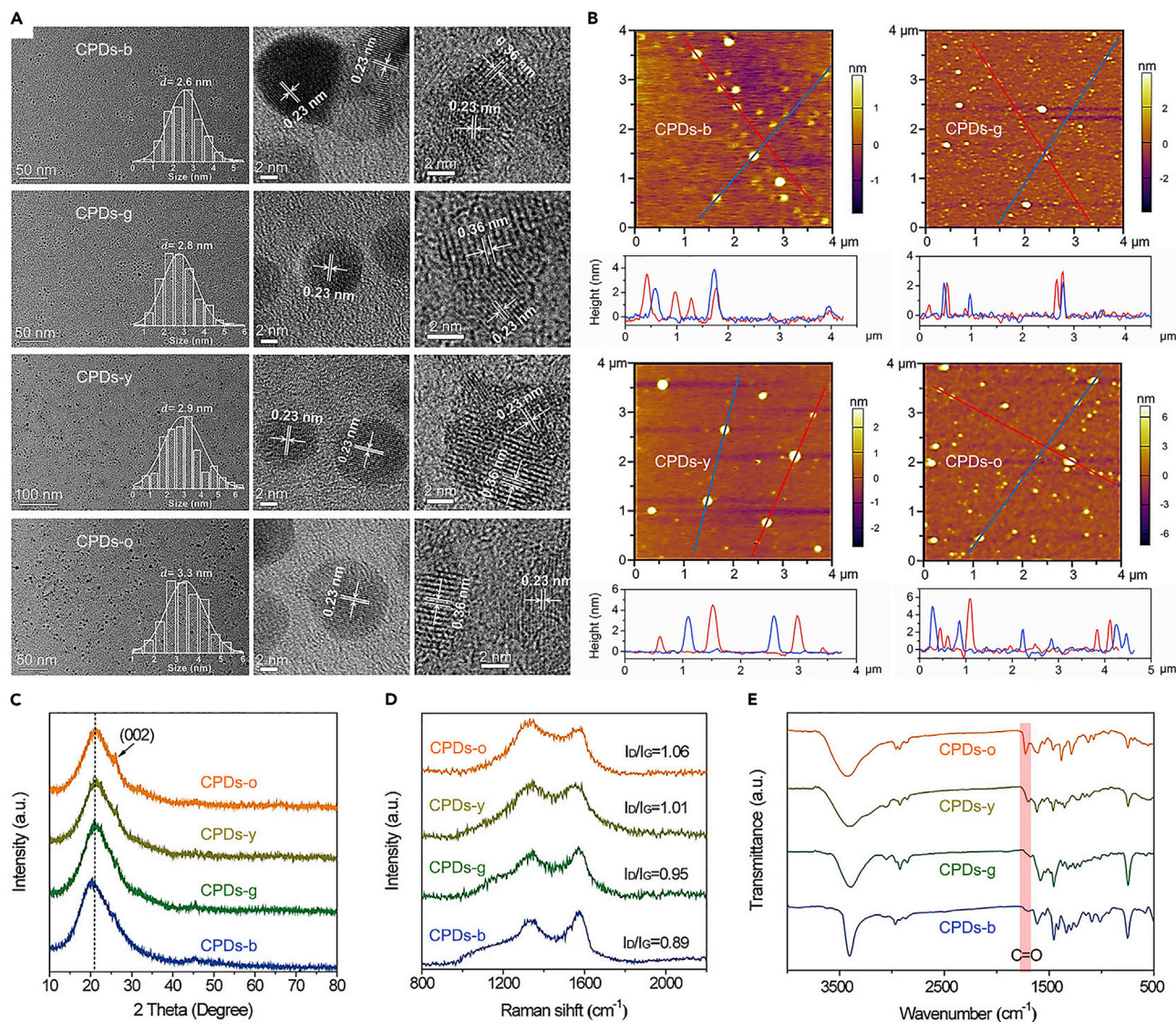
Figure 5. Morphologies and Compositions of CPDs-b, CPDs-g, CPDs-y, and CPDs-o
(A) TEM (left) and high-resolution-TEM (middle and right) images of the four CPDs; inset: particle size distribution histogram.
(B) Atomic force microscopic images (top) and corresponding particle heights (bottom) of the four CPDs.
(C–E) (C) XRD patterns, (D) Raman spectra, and (E) FTIR spectra of the four CPDs.
See also Table S4 and Figure S9.

relatively pure secondary-amine peaks morphed into composite N−H and O−H peaks. This transition increased polarity, with CPDs-y and CPDs-o exhibiting higher polarities than CPDs-b and CPDs-g (Ding et al., 2016).

The compositions and valence states of these samples were further revealed by X-ray photoelectron spectroscopy (XPS). The full spectra in Figure S9 depict three typical peaks that correspond to C 1s, N 1s, and O 1s states. An increase in the O/C ratio, from 0.09 to 0.17, 0.20, and 0.24 was the most obvious change observed in the XPS spectrum in moving from CPDs-b to CPDs-g, CPDs-y, and CPDs-o, consistent with an increase in the oxygen content. The high-resolution XPS spectra reveal that the C 1s band can be deconvoluted into four peaks assigned to C=C/C−C (284.0–284.4 eV), C−N (284.8–285.2 eV), C−O (286.0–286.3 eV), and C=O (288.3–288.5 eV) groups (Ding et al., 2016). The N 1s band could also be split into pyrrolic N (399.3 eV) and graphitic N (400.8 eV) (Hola et al., 2017), whereas the O 1s spectra revealed
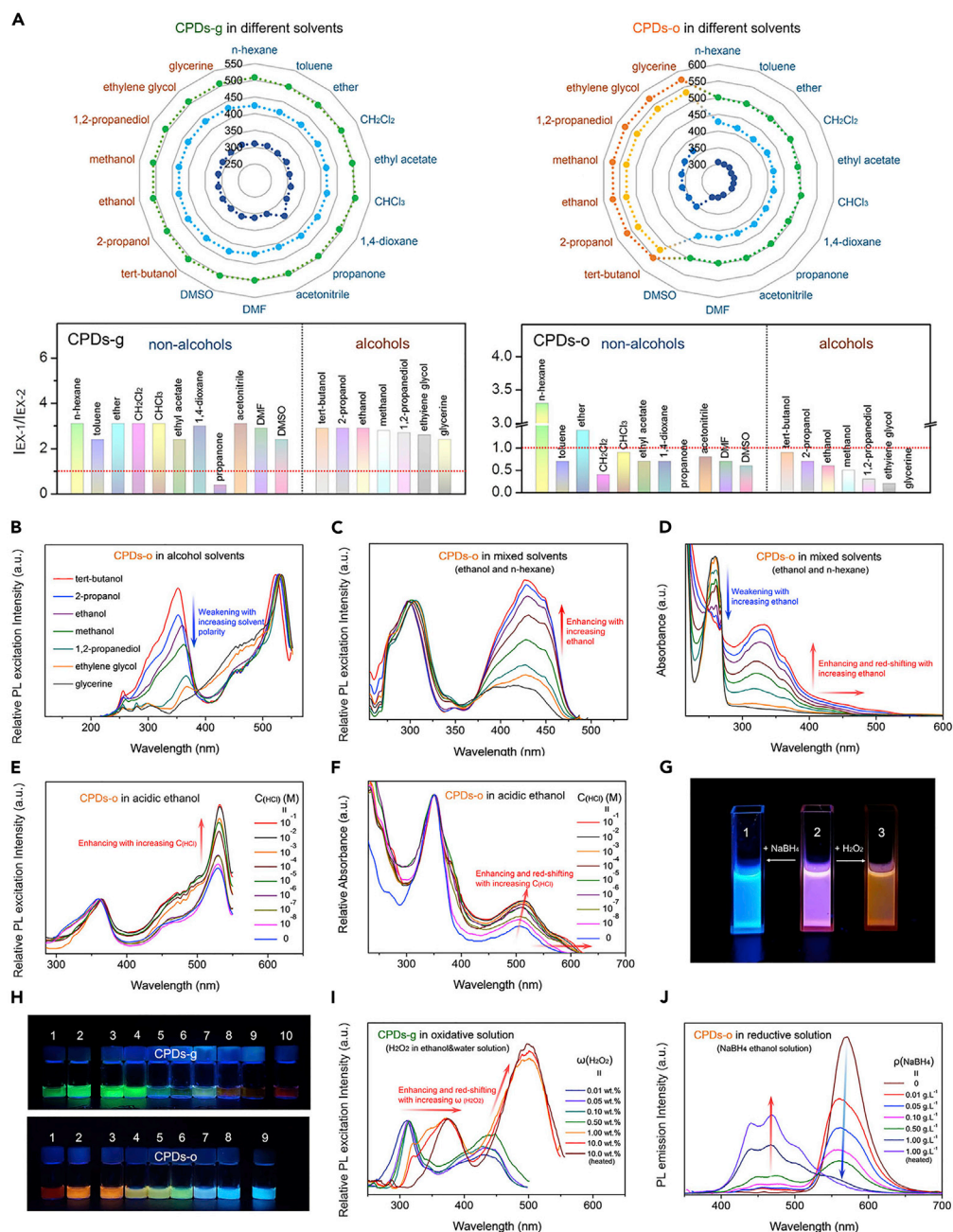
Figure 6. The Effect of Solvent, Acidity, and Redox Conditions on CPDs-g and CPDs-o

(A) Comparing data for CPDs-g and CPDs-o in various solvents, including Ex-1, Ex-2, and Em peak values (inner, middle, and outer rings on the radar maps, respectively) and histograms of Ex-1/Ex-2 intensity ratios, which are related to Tables S5 and S6.

(B) Relative optimum excitation spectra of CPDs-o in various alcohols with 494–508-nm PL emission (all Ex-2 intensities are set to a fixed value).

(C) Relative optimum excitation spectra of CPDs-o in a mixed solvent of n-hexane and ethanol with 500–506-nm PL emission (all Ex-1 intensities are set to a fixed value).

(D) UV-visible absorption spectra of CPDs-o in a mixed solvent of n-hexane and ethanol.

(E) Relative optimum excitation spectra of CPDs-o in acidic ethanol with 506–508-nm PL emission (all Ex-1 intensities are set to a fixed value).

(F) Relative UV-visible absorption spectra of CPDs-o in acidic ethanol (all Abs-1 intensities are set to a fixed value).

Figure 6. *Continued*

(G) Photographic image of the crude reaction products (diluted thirty-times with ethanol) formed by the addition of excess $NaBH_4$ and H_2O_2 when excited using 365-nm UV light.

(H) Photographic images showing the effect of the redox conditions on CPDs-g and CPDs-o when excited with 365-nm UV. For CPDs-g: sample 1 is a heated CPDs-g/$NaBH_4$ solution [$\rho(NaBH_4)$ = 1 g.L^{-1}]; sample 2 is an unheated CPDs-g/$NaBH_4$ solution (ρ = 1 g.L^{-1}); samples 3–9 are CPDs-g/H_2O_2 solutions in ethanol/water with H_2O_2 dosages of 0, 0.01, 0.05, 0.1, 0.5, 1, 10 wt %; and sample 10 is a heated CPDs-g/H_2O_2 solution [$\omega(H_2O_2)$ = 10 wt %]. For CPDs-o: sample 1 is a heated CPDs-o/H_2O_2 solution [$\omega(H_2O_2)$ = 1 wt %]; sample 2 is an unheated CPDs-o/H_2O_2 solution (ω = 1 wt %); samples 3–8 are CPDs-o/$NaBH_4$ solutions in ethanol with $NaBH_4$ dosages of 0 0.01, 0.05, 0.1, 0.5, and 1 g.L^{-1}; and sample 9 is a heated CPDs-o/$NaBH_4$ solution [$\rho(NaBH_4)$ = 1 g.L^{-1}].

(I) Relative optimum excitation spectra of CPDs-g in oxidative solutions with 508–572-nm PL emission (all Ex-1 intensities are set to a fixed value).

(J) Emission spectra of CPDs-o in reductive solutions excited at 338 nm.

See also Tables S5–S9 and Figures S10–S23.

the existence of C−O and C=O groups at 536.1 and 532.9 eV, respectively. The relevant data in Table S4 show that the proportion of C=O in the C 1s spectrum increased from 1% (CPDs-b) to 4% (CPDs-g), 7% (CPDs-y), and 9% (CPDs-o), whereas the analogous O 1s proportions were 60% (CPDs-b), 61% (CPDs-g), 73% (CPDs-y), and 82% (CPDs-o). In addition, as revealed by the N 1s data, the proportion of graphitic N increases from 4% (CPDs-b) to 5% (CPDs-g), 8% (CPDs-y), and 14% (CPDs-o), consistent with an increasing number of N atoms imbedded in the sp^2 scaffold, indicating that N-based groups are other important emission centers. The graphitic N evidently triggers redshifts in the absorption spectra of CPDs due to its electron-doping effect that reduces the electronic gap and systematically transforms energy levels (Sarkar et al., 2016), whereas the pyridinic or pyrrolic N has the opposite effect (Sudolska and Otyepka, 2017). In summary, an increase in graphitic N is the immediate reason for the redshift observed for the Abs-1 peaks, and indirectly led to Ex-1 peaks with longer wavelengths.

Further Evidence in Support of the CPD PL Mechanism
Solvent Effect

As mentioned in the preceding section, the I_{Ex-2}/I_{Ex-1} and I_{Em-2}/I_{Em-1} ratios increased with increasing fluorescence redshift, which indicates that the contribution of the surface structure to PL emission increased in moving from CPDs-b to CPDs-g, CPDs-y, and CPDs-o. To confirm that the emission centers are N/O-based groups, several sets of experiment were designed in which the solvent, acidity/alkalinity, and redox conditions were rationally altered to effectively adjust the surface chemical groups. Here, CPDs-g and CPDs-o were chosen as model samples because they exhibit markedly different I_{Ex-2}/I_{Ex-1} and I_{Em-2}/I_{Em-1} ratios, PL colors, and surface functional groups.

Figure S10 reveals that CPDs-g emitted similar blue-green PL in various solvents, whereas CPDs-o presented blue-yellow PL in non-alcoholic solvents but yellow-orange PL in alcoholic solvents. Specific data are shown in Figures 6A, S11, and S12 and Tables S5 and S6. CPDs-g exhibited similar Em wavelengths in various solvents (except propanone) that ranged from 492 to 508 nm, whereas the Ex-1 wavelength ranged from 306 to 313 nm and the Ex-2 wavelength ranged from 412 to 430 nm; the I_{Ex-1}/I_{Ex-2} values of 2.4–3.1 were observed and displayed slight changes. Conversely, CPDs-o showed significantly different optical properties in non-alcoholic and alcoholic solutions. In non-alcoholic solvents (except propanone), the Em, Ex-1, Ex-2, and I_{Ex-1}/I_{Ex-2} values of CPDs-o were observed to be 492–500 nm, 295–303 nm, 415–427 nm, and 0.6–3.3 respectively, whereas in alcoholic solvents (except glycerine), CPDs-o was yellow-orange with longer-wavelength PLs that ranged from 553 to 573 nm, Ex-1 values of 351–368 nm, Ex-2 at 553–573 nm, and I_{Ex-1}/I_{Ex-2} that ranged from 0.2 to 0.9. These results demonstrate that alcoholic solvents more strongly affect CPDs-o, which indicates that CPDs-o possesses more surface states (that is, oxygen- and nitrogen-based groups). Moreover, the I_{Ex-1}/I_{Ex-2} ratios of both CPDs tended to decrease with increasing polarity or proportion of hydroxyl groups present in the alcoholic solvent. For CPDs-g, the value decreased slightly, from 2.9 to 2.4, as the solvent was changed from *tert*-butanol to glycerine, whereas the value decreased sharply for CPDs-o, from 0.9 to 0.2, with the same solvent change (the Ex-1 peak of CPDs-o disappeared in glycerine). In other words, the Ex-2 intensity increased with the increasing proportion of hydroxyl groups in the alcoholic solvent (Figure 6B). More evidence is provided by the photographic image, and the Ex and Em spectra of CPDs-o in mixed solutions of n-hexane and ethanol with different volume ratios (Figures S13 and S14, and Table S7). It was observed that these solutions emitted blue-green light (500–506 nm) when excited by 365-nm UV light, with the I_{Ex-1}/I_{Ex-2} ratio decreasing from 3.3 to 0.6 with

increasing ethanol concentrations (Figure 6C). Changes in the absorption peaks shown in Figure 6D can explain the above-mentioned observations; the Abs-1 intensity decreased, whereas Abs-2 increased, and the absorption edge redshifted with increasing ethanol concentrations, indicating that the alcohol hydroxyl group promoted energy absorption from the surface groups, which resulted in Ex-2 peak enhancement and a redshift in the PL emission.

The Effect of Acidity/Basicity

As shown in Figures S15A and S16, and Table S8, CPDs-g emitted green (508 nm) PL in alkaline (NaOH concentration (C_{NaOH}) of between 0 and 10^{-1} mol.L^{-1}) and weakly acidic (C_{HCl} of between 10^{-7} and 5×10^{-6} mol.L^{-1}) ethanol, but pink PL (mixture of emissions at 380, 442, 569, and 610 nm) in strongly acidic ethanol (C_{HCl} between 10^{-5} and 10^{-1} mol.L^{-1}). The Abs spectrum of CPDs-g in ethanol (Figure S17) is bimodal, with peaks at 302 and 422 nm, but transformed into a multimodal spectrum with four peaks (306, 365, 493, and 573 nm) as the HCl concentration was increased to 10^{-5} mol.L^{-1}. Acid promotes protonation, which boosts the long-wavelength emission. However, CPDs-g exhibited a full width at half maximum of ~200 nm, which indicates that CPDs-g had relatively impure emission centers. Consequently, HCl could only partially protonate CPDs-g to produce CPDs that emitted at 569 and 610, with the original blue-green emission of the impure CPDs-g also retained.

In sharp contrast, Figure S15B and S18 and Table S9 revealed that CPDs-o emitted orange PL (~570 nm) in acidic ethanol (C_{HCl} range: 0 to 10^{-1} mol.L^{-1}) but blue-yellow PL in alkaline ethanol (C_{NaOH} range: 10^{-7} to 10^{-1} mol.L^{-1}). The longer-wavelength emissions (560–570 nm) disappeared, whereas the shorter-wavelength emissions (390, ~508 nm) strengthened with increasing C_{NaOH}, revealing that OH^--induced deprotonation suppressed long-wavelength emissions. The data displayed in Figure S19 can be used to explain the above-mentioned observations, namely, the OH^- suppressed absorbance of energy from the surface groups and caused all Abs peaks to be blueshifted and weakened. Also, protonation enhanced the Abs-2 peaks (Figure 6F) and promoted the contributions of surface structures to PL emission (Figure 6E), thereby reducing I_{Ex-1}/I_{Ex-2} from 0.64 to 0.35.

Redox Conditions

As depicted in Figure 6G, blue or orange-red PL color was observed when excess $NaBH_4$ or H_2O_2 was added to the crude reaction product. The Em spectra in Figure S20 show that the reducing reagent ($NaBH_4$) destroyed the long-wavelength-emitting part of the original CPD. In contrast, an oxidizing reagent (H_2O_2) decreased the short-wavelength-emitting part of the original CPD (Figure S20C). Therefore, CPDs-g, with low surface oxidation, can be considered to contain reduced CPDs, whereas CPDs-o, with high surface oxidation, can be considered to contain oxidized CPDs, hence they can further react with $NaBH_4$ or H_2O_2. Figures 6H (top), 6I, and S21 reveal that samples 3 to 9, which are CPDs-g samples in 0, 0.01, 0.05, 0.1, 0.5, 1, and 10 wt % H_2O_2 solutions, respectively, displayed PL colors that were increasingly redshifted with increasing H_2O_2 concentrations, and sample 10, which was heated and is more oxidized, emitted stronger red light. Conversely, CPDs-g still maintained its green PL in $NaBH_4$ solution (samples 1 and 2), irrespective of whether it was heated or not, which indicates that CPDs-g cannot be reduced. In sharp contrast, Figures 6H (bottom), 6J, and S22 reveal that samples 3 to 8, which are CPDs-o samples in 0 0.01, 0.05, 0.1, 0.5, and 1.0 g.L^{-1} $NaBH_4$ solutions, respectively, displayed PL colors that were increasingly blueshifted with increasing $NaBH_4$ concentrations, and sample 9, which was heated and is more reduced, emits stronger blue light. CPDs-o still maintained its orange PL in H_2O_2 solution, which indicates that CPDs-o is insensitive to oxidation (sample 2).

DISCUSSION

The study is novel in that it describes the simple, effective, and high-yielding preparation of a full-color palette of fluorescent CPDs and an investigation into their fluorescence mechanism. The study showed that the quasi-spherical CPDs are composed of compact graphitic cores with surface N/O functional groups. Despite many efforts, there is still considerable debate surrounding the light-absorption and fluorescence-generating mechanisms of CPDs. Reasonable mechanisms include the sp^2-conjugated carbon-core state and the surface state (Wu et al., 2017b; Liu et al., 2019). The absorption of the carbon-core state stems from π-π^* transitions of C=C bonds, and a PL redshift is realized through quantum size effects achieved by manipulating the size of the carbon core (Kim et al., 2012). Conversely, the surface state mainly absorbs through n–π^* transitions of functional groups or doped heteroatoms that determine the PL

emission (Liu et al., 2015a). In addition, a small number of articles have reported synergism brought on by both core and surface states (Miao et al., 2018; Bao et al., 2015). The molecular state has also been confirmed in citric acid-derived CDs (Song et al., 2015). In this study, the fluorescence properties appear to depend mainly on the surface state, with N-doping (that is, graphitic N) or graphitization in the core state possibly causing the absorption of the core to redshift. In other words, regardless of which energy level an excited electron is in, it may ultimately relax into the lowest unoccupied molecular orbital (LUMO) band of the surface state, after which it returns to the highest occupied molecular orbital (HOMO) band (ground state). Therefore, the HOMO-LUMO band gap of the surface state is a determining factor for PL generation. Surface oxidation or functionalization is regarded to be an effective method for roughly controlling the band gap. The band gap narrows as an increasing number of C=O groups and oxygen atoms merge in the surface structure, which is possibly due to the appearance of new sub-levels that give rise to a PL redshift (Bao et al., 2011; Sudolska et al., 2015).

The as-prepared CPDs, especially CPDs-g, are also water-soluble, as shown in Figure S23; an aqueous CPDs-g solution exhibited very similar PL behavior to CPDs-g in ethanol, which eliminates solubility concerns associated with adopting these CPDs for bioimaging and biodetection purposes. The present results also provide extra evidence for the cross-link-enhanced emission effect (Zhu et al., 2014). As both cationic polymerization and oxidation reactions contribute to building the main CPD framework, the emission centers of the final CPDs were confirmed to be oxygen- and nitrogen-based groups that are fixed by cross-linked polymer structures.

Conclusion

We believe that our study makes a contribution to the literature because it describes the simple, effective, and high-yielding preparation of a full-color palette of fluorescent CPDs, and investigates their formation and fluorescence mechanism. The study showed that the quasi-spherical CPDs are composed of compact graphitic cores with surface N/O functional groups. During their formation, polymerization may provide the organic skeleton and oxidation and solvothermal carbonization led to the heterogeneous surface state. In addition, energy could be absorbed by the carbon core and the surface groups at the same time, and is then transferred to the unique emissive site, resulting in the emission of PL.

Limitations of the Study

We still lack an efficient route to outline the precise chemical structures of multicolor-emissive CPDs. Although the synthesized CPDs are quantitatively sensitive to pH, solvent, and oxidizer/reductant, the exact relationship between the chemical structures of CPDs and optical information/PL mechanism is insufficient.

Resource Availability

Lead Contact

Further information and requests for resources and reagents should be directed to and will be fulfilled by the Lead Contact, Jiucun Chen (chenjc@swu.edu.cn).

Materials Availability

All unique/stable reagents generated in this study are available from the Lead Contact without restriction.

Data and Code Availability

All relevant data are available from the corresponding author (chengzhi@swu.edu.cn; sjzhu@jlu.edu.cn; chenjc@swu.edu.cn) upon reasonable request.

METHODS

All methods can be found in the accompanying Transparent Methods supplemental file.

SUPPLEMENTAL INFORMATION

Supplemental Information can be found online at https://doi.org/10.1016/j.isci.2020.101546.

CellPress
OPEN ACCESS

AUTHOR CONTRIBUTIONS

C.H., S.Z., and J.C. conceived and supervised the research. C.L. performed all the experiments. Y.J., R.W., T.H., X.L., and B.W. helped to perform biology experiments. C.L. wrote the manuscript.

DECLARATION OF INTERESTS

The authors declare no competing interests.

REFERENCES

Bao, L., Liu, C., Zhang, Z.L., and Pang, D.W. (2015). Photoluminescence-tunable carbon nanodots: surface-state energy-gap tuning. Adv. Mater. 27, 1663–1667.

Bao, L., Zhang, Z.L., Tian, Z.Q., Zhang, L., Liu, C., Lin, Y., Qi, B., and Pang, D.W. (2011). Electrochemical tuning of luminescent carbon nanodots: from preparation to luminescence mechanism. Adv. Mater. 23, 5801–5810.

Deng, Z., Liu, C., Jin, Y., Pu, J., Wang, B., and Chen, J. (2019). High quantum yield blue- and orange-emitting carbon dots: one-step microwave synthesis and applications as fluorescent films and in fingerprint and cellular imaging. Analyst 144, 4569–4574.

Ding, H., Yu, S.B., Wei, J.S., and Xiong, H.M. (2016). Full-color light-emitting carbon dots with a surface-state-controlled luminescence mechanism. ACS Nano 10, 484–491.

Dong, Y., Pang, H., Yang, H.B., Guo, C., Shao, J., Chi, Y., Li, C.M., and Yu, T. (2013). Carbon-based dots co-doped with nitrogen and sulfur for high quantum yield and excitation-independent emission. Angew. Chem. Int. Ed. 52, 7800–7804.

Gao, D., Zhao, H., Chen, X., and Fan, H. (2018a). Recent advance in red-emissive carbon dots and their photoluminescent mechanisms. Mater. Today Chem. 9, 103–113.

Gao, W., Song, H., Wang, X., Liu, X., Pang, X., Zhou, Y., Gao, B., and Peng, X. (2018b). Carbon dots with red emission for sensing of Pt^{2+}, Au^{3+}, and Pd^{2+} and their bioapplications in vitro and in vivo. ACS Appl. Mater. Inter. 10, 1147–1154.

Ge, J., Jia, Q., Liu, W., Guo, L., Liu, Q., Lan, M., Zhang, H., Meng, X., and Wang, P. (2015). Red-emissive carbon dots for fluorescent, photoacoustic, and thermal theranostics in living mice. Adv. Mater. 27, 4169–4177.

Han, L., Liu, S.G., Dong, J.X., Liang, J.Y., Li, L.J., Li, N.B., and Luo, H.Q. (2017). Facile synthesis of multicolor photoluminescent polymer carbon dots with surface-state energy gap-controlled emission. J. Mater. Chem. C 5, 10785–10793.

Hola, K., Sudolska, M., Kalytchuk, S., Nachtigallova, D., Rogach, A.L., Otyepka, M., and Zboril, R. (2017). Graphitic nitrogen triggers red fluorescence in carbon dots. ACS Nano 11, 12402–12410.

Hola, K., Zhang, Y., Wang, Y., Giannelis, E.P., Zboril, R., and Rogach, A.L. (2014). Carbon dots-emerging light emitters for bioimaging, cancer therapy and optoelectronics. Nano Today 9, 590–603.

Jiang, K., Sun, S., Zhang, L., Lu, Y., Wu, A., Cai, C., and Lin, H. (2015). Red, green, and blue luminescence by carbon dots: full-color emission tuning and multicolor cellular imaging. Angew. Chem. Int. Ed. 54, 5360–5363.

Jiang, K., Wang, Y., Cai, C., and Lin, H. (2018). Conversion of carbon dots from fluorescence to ultralong room-temperature phosphorescence by heating for security applications. Adv. Mater. 30, 3104–3112.

Kim, S., Choi, Y., Park, G., Won, C., Park, Y.J., Lee, Y., Kim, B.S., and Min, D.H. (2017). Highly efficient gene silencing and bioimaging based on fluorescent carbon dots in vitro and in vivo. Nano Res. 10, 503–519.

Kim, S., Hwang, S.W., Kim, M.K., Shin, D.Y., Shin, D.H., Kim, C.O., Yang, S.B., Park, J.H., Hwang, E., Choi, S.H., et al. (2012). Anomalous behaviors of visible luminescence from graphene quantum dots: interplay between size and shape. ACS Nano 6, 8203–8208.

Koiry, S.P., Saxena, V., Sutar, D., Bhattacharya, S., Aswal, D.K., Gupta, S.K., and Yakhmi, J.V. (2007). Interfacial synthesis of long polyindole fibers. J. Appl. Polym. Sci. 103, 595–599.

Kong, B., Tang, J., Zhang, Y., Jiang, T., Gong, X., Peng, C., Wei, J., Yang, J., Wang, Y., Wang, X., et al. (2016). Incorporation of well-dispersed sub-5-nm graphitic pencil nanodots into ordered mesoporous frameworks. Nat. Chem. 8, 171–178.

Kong, B., Zhu, A., Ding, C., Zhao, X., Li, B., and Tian, Y. (2012). Carbon dot-based inorganic-organic nanosystem for two-photon imaging and biosensing of pH variation in living cells and tissues. Adv. Mater. 24, 5844–5848.

Li, D., Jing, P., Sun, L., An, Y., Shan, X., Lu, X., Zhou, D., Han, D., Shen, D., Zhai, Y., et al. (2018a). Near-infrared excitation/emission and multiphoton-induced fluorescence of carbon dots. Adv. Mater. 30, 1705913.

Li, F., Li, T., Sun, C., Xia, J., Jiao, Y., and Xu, H. (2017). Selenium-doped carbon quantum dots for free-radical scavenging. Angew. Chem. Int. Ed. 56, 9910–9914.

Li, J., Yang, S., Deng, Y., Chai, P., Yang, Y., He, X., Xie, X., Kang, Z., Ding, G., Zhou, H., and Fan, X. (2018b). Emancipating target-functionalized carbon dots from autophagy vesicles for a novel visualized tumor therapy. Adv. Funct. Mater. 28, 1800881.

Liu, C., Wang, R., Wang, B., Deng, Z., Jin, Y., Kang, Y., and Chen, J. (2018). Orange, yellow and blue luminescent carbon dots controlled by surface state for multicolor cellular imaging, light emission and illumination. Microchim. Acta 185, 539.

Liu, H., He, Z., Jiang, L.P., and Zhu, J.J. (2015a). Microwave-assisted synthesis of wavelength-tunable photo luminescent carbon nanodots and their potential applications. ACS Appl. Mater. Inter. 7, 4913–4920.

Liu, J., Liu, Y., Liu, N., Han, Y., Zhang, X., Huang, H., Lifshitz, Y., Lee, S.T., Zhong, J., and Kang, Z. (2015b). Metal-free efficient photocatalyst for stable visible water splitting via a two-electron pathway. Science 347, 970–974.

Liu, M.L., Chen, B.B., Li, C.M., and Huang, C.Z. (2019). Carbon dots: synthesis, formation mechanism, fluorescence origin and sensing applications. Green Chem. 21, 449–471.

Liu, Y., Tian, Y., Tian, Y., Wang, Y., and Yang, W. (2015c). Carbon-dot-based nanosensors for the detection of intracellular redox state. Adv. Mater. 27, 7156–7160.

Miao, X., Qu, D., Yang, D., Nie, B., Zhao, Y., Fan, H., and Sun, Z. (2018). Synthesis of carbon dots with multiple color emission by controlled graphitization and surface functionalization. Adv. Mater. 30, 1704740.

Nie, H., Li, M., Li, Q., Liang, S., Tan, Y., Sheng, L., Shi, W., and Zhang, S.X.A. (2014). Carbon dots with continuously tunable full-color emission and their application in ratiometric pH sensing. Chem. Mater. 26, 3104–3112.

Pansare, V.J., Hejazi, S., Faenza, W.J., and Prud'homme, R.K. (2012). Review of long-wavelength optical and NIR imaging materials: contrast agents, fluorophores, and multifunctional nano carriers. Chem. Mater. 24, 812–827.

Phasuksom, K., and Sirivat, A. (2016). Synthesis of nano-sized polyindole via emulsion polymerization and doping. Synth. Met. 219, 142–153.

Qu, S., Wang, X., Lu, Q., Liu, X., and Wang, L. (2012). A biocompatible fluorescent ink based on water-soluble luminescent carbon nanodots. Angew. Chem. Int. Ed. 51, 12215–12218.

Sarkar, S., Sudolska, M., Dubecky, M., Reckmeier, C.J., Rogach, A.L., Zboril, R., and Otyepka, M. (2016). Graphitic nitrogen doping in carbon dots causes red-shifted absorption. J. Phys. Chem. C 120, 1303–1308.

Siddiquee, M.N., and de Klerk, A. (2015). Heterocyclic addition reactions during low temperature autoxidation. Energ. Fuel. 29, 4236–4244.

Song, Y., Zhu, S., Zhang, S., Fu, Y., Wang, L., Zhao, X., and Yang, B. (2015). Investigation from chemical structure to photoluminescent mechanism: a type of carbon dots from the pyrolysis of citric acid and an amine. J. Mater. Chem. C 3, 5976–5984.

Soylu, O., Uzun, S., and Can, M. (2011). The investigation of acid effect on chemical polymerization of indole. Colloid Polym. Sci. 289, 903–909.

Speicher, A., Eicher, T., and Hauptmann, S. (2012). The Chemistry of Heterocycles: Structures, Reactions, Synthesis, and Applications (Wiley-VCH Verlag GmbH), pp. 108–147.

Sudolska, M., Dubecky, M., Sarkar, S., Reckmeier, C.J., Zboril, R., Rogach, A.L., and Otyepka, M. (2015). Nature of absorption bands in oxygen-functionalized graphitic carbon dots. J. Phys. Chem. C 119, 13369–13373.

Sudolska, M., and Otyepka, M. (2017). Exact roles of individual chemical forms of nitrogen in the photoluminescent properties of nitrogen-doped carbon dots. Appl. Mater. Today 7, 190–200.

Sun, C.L., and Shi, Z.J. (2014). Transition-metal-free coupling reactions. Chem. Rev. 114, 9219–9280.

Sun, S., Zhang, L., Jiang, K., Wu, A., and Lin, H. (2016). Toward high-efficient red emissive carbon dots: facile preparation, unique properties, and applications as multifunctional theranostic agents. Chem. Mater. 28, 8659–8668.

Sun, X., Brueckner, C., and Lei, Y. (2015). One-pot and ultrafast synthesis of nitrogen and phosphorus co-doped carbon dots possessing bright dual wavelength fluorescence emission. Nanoscale 7, 17278–17282.

Tao, H., Yang, K., Ma, Z., Wan, J., Zhang, Y., Kang, Z., and Liu, Z. (2012). In vivo NIR fluorescence imaging, biodistribution, and toxicology of photoluminescent carbon dots produced from carbon nanotubes and graphite. Small 8, 281–290.

Tao, S., Feng, T., Zheng, C., Zhu, S., and Yang, B. (2019). Carbonized polymer dots: a brand new perspective to recognize luminescent carbon-based nanomaterials. J. Phys. Chem. Lett. 10, 5182–5188.

Tiwari, M., Kumar, A., Umre, H.S., and Prakash, R. (2015). Microwave-assisted chemical synthesis of conducting polyindole: study of electrical property using Schottky junction. J. Appl. Polym. Sci. 132, 42192.

Wang, F., Xie, Z., Zhang, H., Liu, C.Y., and Zhang, Y.G. (2011). Highly luminescent organosilane-functionalized carbon dots. Adv. Funct. Mater. 21, 1027–1031.

Wang, Z., Yuan, F., Li, X., Li, Y., Zhong, H., Fan, L., and Yang, S. (2017). 53% efficient red emissive carbon quantum dots for high color rendering and stable warm white-light-emitting diodes. Adv. Mater. 29, 1702910.

Wu, M., Zhan, J., Geng, B., He, P., Wu, K., Wang, L., Xu, G., Li, Z., Yin, L., and Pan, D. (2017a). Scalable synthesis of organic-soluble carbon quantum dots: superior optical properties in solvents, solids, and LEDs. Nanoscale 9, 13195–13202.

Wu, Z.L., Liu, Z.X., and Yuan, Y.H. (2017b). Carbon dots: materials, synthesis, properties and approaches to long-wavelength and multicolor emission. J. Mater. Chem. B 5, 3794–3809.

Xia, C., Zhu, S., Feng, T., Yang, M., and Yang, B. (2019). Evolution and synthesis of carbon dots: from carbon dots to carbonized polymer dots. Adv. Sci. 6, 1901316.

Xiong, Y., Schneider, J., Ushakova, E.V., and Rogach, A.L. (2018). Influence of molecular fluorophores on the research field of chemically synthesized carbon dots. Nano Today 23, 124–139.

Yang, C., Zhu, S., Li, Z., Li, Z., Chen, C., Sun, L., Tang, W., Liu, R., Sun, Y., and Yu, M. (2016).

Nitrogen-doped carbon dots with excitation-independent long-wavelength emission produced by a room-temperature reaction. Chem. Commun. 52, 11912–11914.

Yang, H., Liu, Y., Guo, Z., Lei, B., Zhuang, J., Zhang, X., Liu, Z., and Hu, C. (2019). Hydrophobic carbon dots with blue dispersed emission and red aggregation-induced emission. Nat. Commun. 10, 1789.

Yang, L., Jiang, W., Qiu, L., Jiang, X., Zuo, D., Wang, D., and Yang, L. (2015). One pot synthesis of highly luminescent polyethylene glycol anchored carbon dots functionalized with a nuclear localization signal peptide for cell nucleus imaging. Nanoscale 7, 6104–6113.

Yeh, T.F., Huang, W.L., Chung, C.J., Chiang, I.T., Chen, L.C., Chang, H.Y., Su, W.C., Cheng, C., Chen, S.J., and Teng, H. (2016). Elucidating quantum confinement in graphene oxide dots based on excitation-wavelength-independent photoluminescence. J. Phys. Chem. Lett. 7, 2087–2092.

Yuan, F., Li, S., Fan, Z., Meng, X., Fan, L., and Yang, S. (2016). Shining carbon dots: synthesis and biomedical and optoelectronic applications. Nano Today 11, 565–586.

Yuan, F., Yuan, T., Sui, L., Wang, Z., Xi, Z., Li, Y., Li, X., Fan, L., Tan, Z.A., Chen, A., et al. (2018). Engineering triangular carbon quantum dots with unprecedented narrow bandwidth emission for multicolored LEDs. Nat. Commun. 9, 2249.

Zhao, S., Song, X., Bu, X., Zhu, C., Wang, G., Liao, F., Yang, S., and Wang, M. (2017). Polydopamine dots as an ultrasensitive fluorescent probe switch for Cr(VI) in vitro. J. Appl. Polym. Sci. 134, 44784.

Zheng, M., Liu, S., Li, J., Qu, D., Zhao, H., Guan, X., Hu, X., Xie, Z., Jing, X., and Sun, Z. (2014). Integrating oxaliplatin with highly luminescent carbon dots: an unprecedented theranostic agent for personalized medicine. Adv. Mater. 26, 3554–3560.

Zhu, S., Meng, Q., Wang, L., Zhang, J., Song, Y., Jin, H., Zhang, K., Sun, H., Wang, H., and Yang, B. (2013). Highly photoluminescent carbon dots for multicolor patterning, sensors, and bioimaging. Angew. Chem. Int. Ed. 52, 3953–3957.

Zhu, S., Song, Y., Zhao, X., Shao, J., Zhang, J., and Yang, B. (2015). The photoluminescence mechanism in carbon dots (graphene quantum dots, carbon nanodots, and polymer dots): current state and future perspective. Nano Res. 8, 355–381.

Zhu, S., Wang, L., Zhou, N., Zhao, X., Song, Y., Maharjan, S., Zhang, J., Lu, L., Wang, H., and Yang, B. (2014). The crosslink enhanced emission (CEE) in non-conjugated polymer dots: from the photoluminescence mechanism to the cellular uptake mechanism and internalization. Chem. Commun. 50, 13845–13848.

Supplemental Information

Indole Carbonized Polymer Dots

Boost Full-Color Emission

by Regulating Surface State

Chang Liu, Yanzi Jin, Ruijie Wang, Tianyang Han, Xiangping Liu, Bing Wang, Chengzhi Huang, Shoujun Zhu, and Jiucun Chen
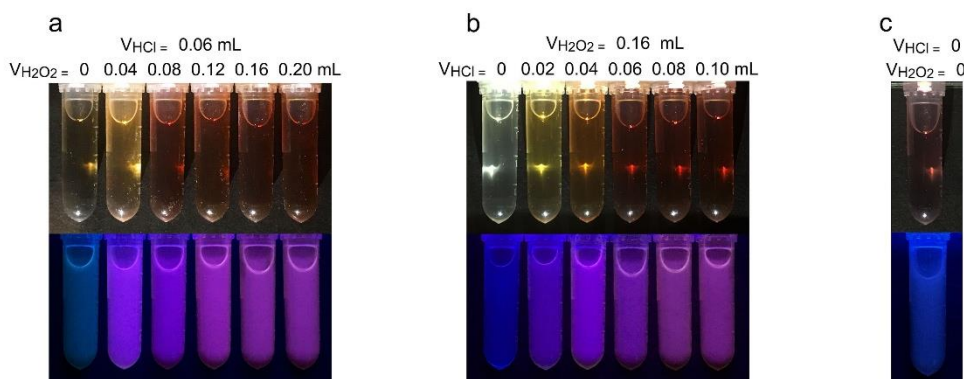
Figure S1 As-prepared reaction mixtures (diluted tenfold by ethanol) under 365 nm UV irradiation. **(a)** These samples were produced by solvothermally treating indole ethanol solution with equivalent HCl (V_{HCl} = 0.06 mL) but tunable doses of H_2O_2 ($V_{H_2O_2}$ from 0 to 0.20 mL). **(b)** These samples were produced by solvothermally treating indole ethanol solution with equivalent H_2O_2 ($V_{H_2O_2}$ = 0.16 mL) but tunable doses of HCl (V_{HCl} from 0 to 0.10 mL). **(c)** This particular sample was produced by solvothermally treating indole ethanol solution without H_2O_2 and HCl. Related to Figure 1
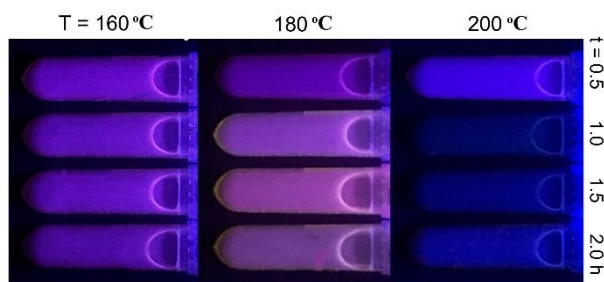

Figure S2 As-prepared reaction mixtures (diluted tenfold by ethanol) under 365 nm UV irradiation. These samples were produced by solvothermally treating the same raw material at different reaction temperatures and time. From left to right, these samples were produced at 160, 180 and 200 °C, respectively; From top to bottom, these samples were obtained after a reaction time of 0.5, 1.0, 1.5 and 2.0 h, respectively. Related to Figure 1
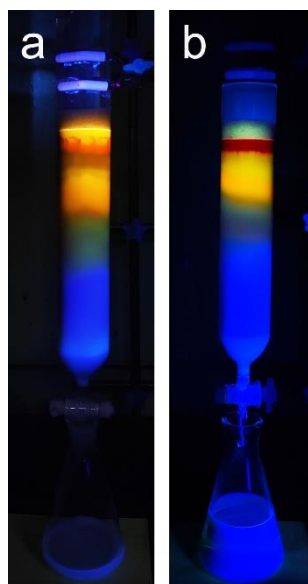
Figure S3 Photograph of the as-prepared reaction mixtures dispersed on silica gel column under 365 nm UV. The eluent is a mixed solvent of ethyl acetate and ethanol. **(a)** The product was obtained from solvothermally treating indole ethanol solution with HCl and tert-butyl peroxide. **(b)** The product was obtained from solvothermally treating indole ethanol solution with both HCl and periodic acid. Related to Figure 1

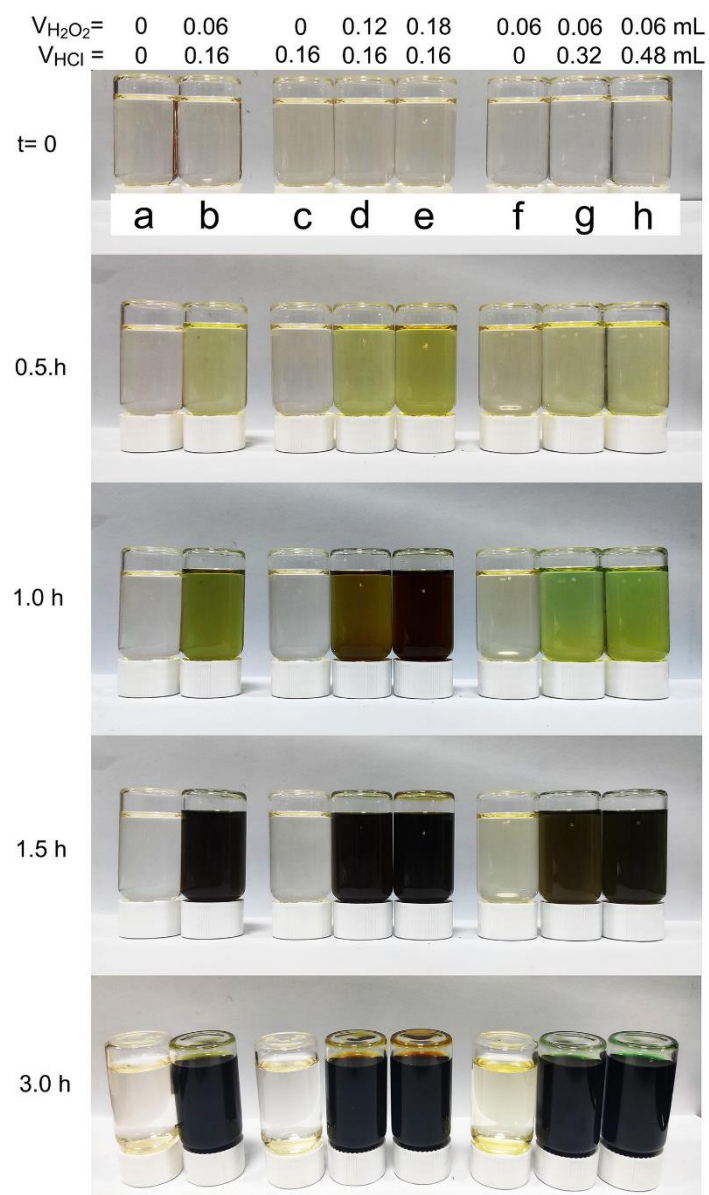**Figure S4** Photograph of freely mixed indole ethanol solution with the adding of HCl and H₂O₂ under normal pressure and room temperature (16 °C). HCl and H₂O₂ would synergistically induce the reaction, and then make the color of solution darker with increasing standing time (from top to bottom). However, such a reaction route can not produce efficient CPDs products. Related to Figure 2
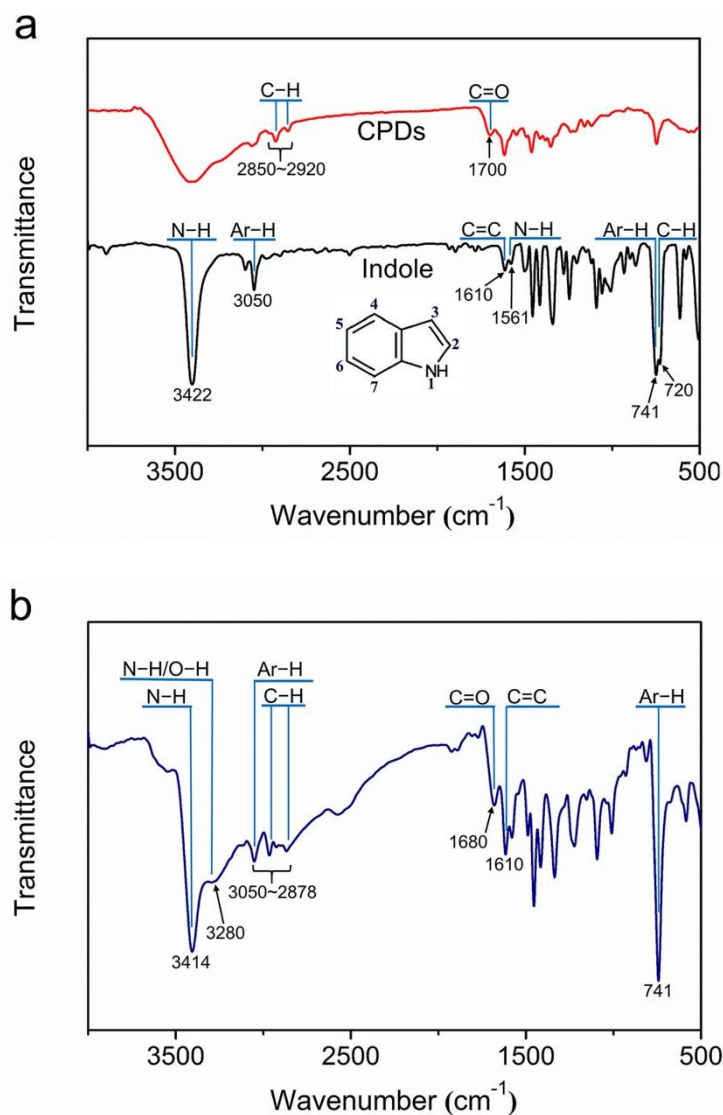
Figure S5 (a) FT-IR spectra of CPDs and indole (the FT-IR curve of CPDs-y was selectively picked up as a particular CPDs' FT-IR spectra). **(b)** FT-IR spectra of the reaction product without solvothermal treatment (the product was directly obtained from the spontaneous reaction happened at indole ethanol solution with the adding of HCl and H_2O_2, corresponding to Supplementary Figure 3b). Related to Figure 2

The structures of the products synthesized at ambient pressure and temperature and without solvothermal treatment lie between those of indole and the CPDs. While the FT-IR spectrum (Figure S5b) shows similar features to those of the CPDs, such as broader N−H/O−H peaks and stronger aliphatic C−H and C=O peaks, characteristics that are more closely related to indole are present in the spectrum, which is ascribable to lack of destruction and reorganization normally caused by the solvothermal

reaction.

It is noteworthy that the N−H groups mainly still exist as secondary (ring) amines, as evidenced by comparing the FT-IR spectra of the CPDs with that of indole (Figure S5), because it is difficult to fragment the pyrrole ring to form a primary amine.
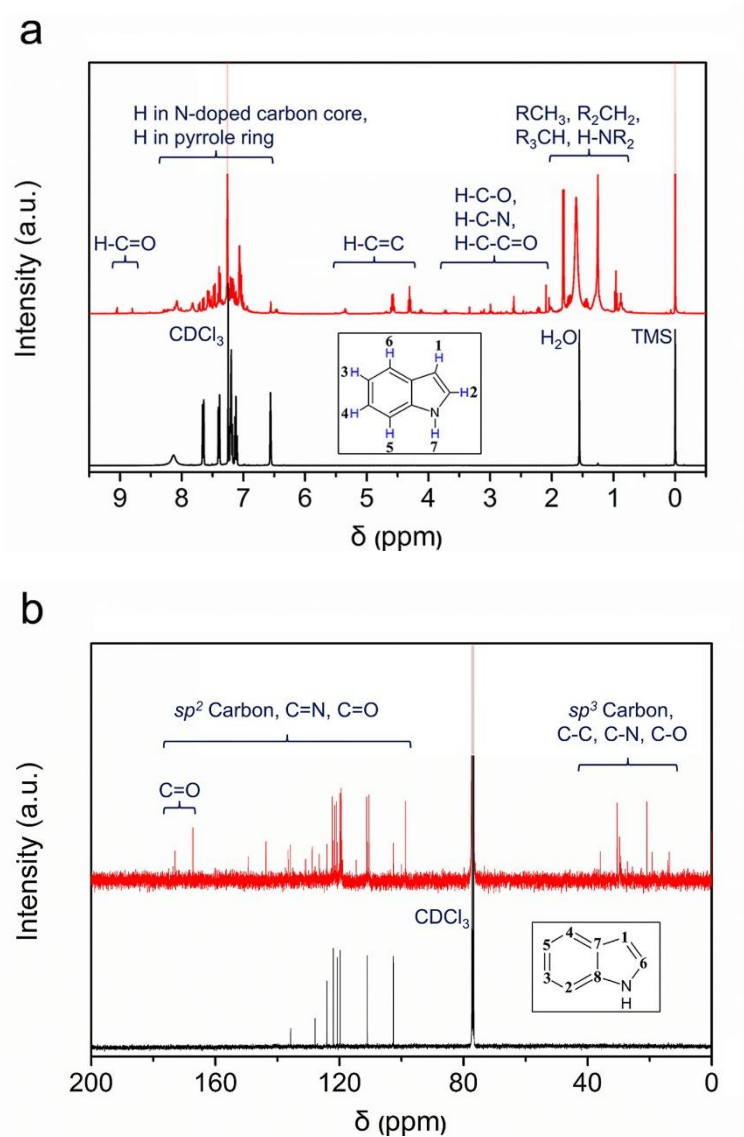
Figure S6 (a) ^{1}H NMR spectra of CPDs (red curve) and indole (black curve) in CDCl$_3$-d (insets: the proposed structure of the CPDs core and surface, the braces marked out the separate regions). **(b)** ^{13}C NMR spectra of CPDs and indole in CDCl$_3$-d (insets: the braces marked out the regions related to carbon different with different molecular orbital). ^{1}H NMR data of indole in CDCl$_3$-d: [1] 6.56 ppm, [2] 7.12 ppm, [3] 7.20 ppm, [4] 7.25 ppm, [5] 7.34 ppm, [6] 7.34 ppm, [7] 8.13 ppm. ^{13}C NMR data of indole in CDCl$_3$-d: [1] 102.64 ppm, [2] 110.99 ppm, [3] 119.81 ppm, [4] 120.73 ppm, [5] 121.98 ppm, [6] 124.09 ppm, [7] 127.84 ppm, [8] 135.77 ppm. Related to Figure 2
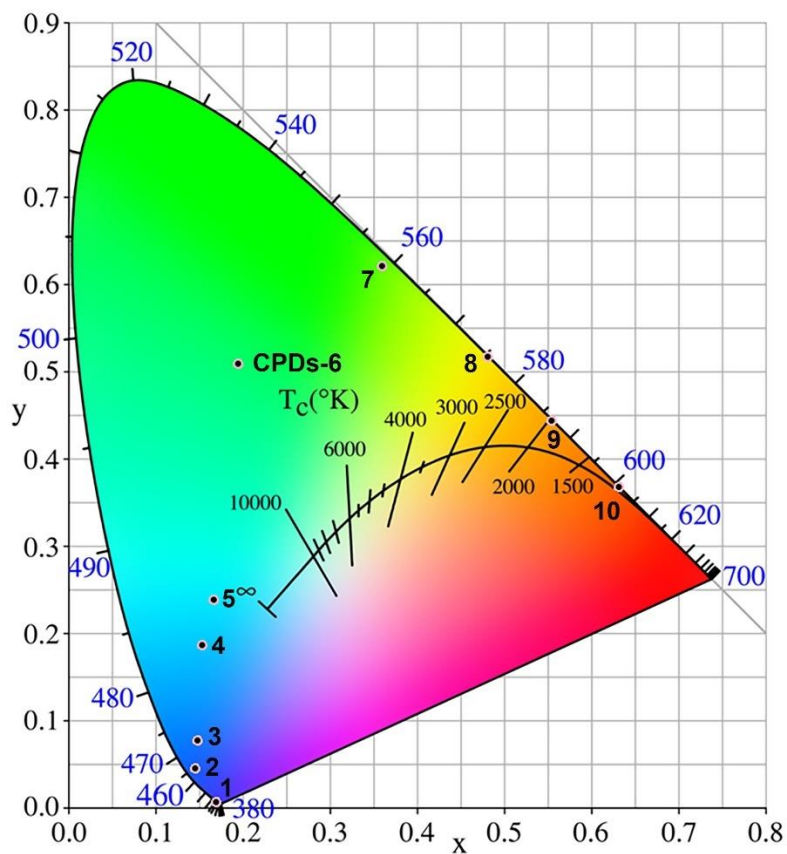
Samples	CIE x	CIE y	Peak (nm)
CPDs-1	0.1698	0.0067	333
CPDs-2	0.1452	0.0451	380
CPDs-3	0.1485	0.0776	416
CPDs-4	0.1527	0.1870	437
CPDs-5	0.1673	0.2382	475
CPDs-6	0.1941	0.5088	508
CPDs-7	0.3602	0.6217	543
CPDs-8	0.4811	0.5170	571
CPDs-9	0.5551	0.4439	587
CPDs-10	0.6320	0.3676	608

Figure S7 Commission International de I' Eclairage (CIE) color coordinate of ten samples. The photograph was composed by using professional software (CIE1931xy.V.1.6.0.2). Related to Figure 3
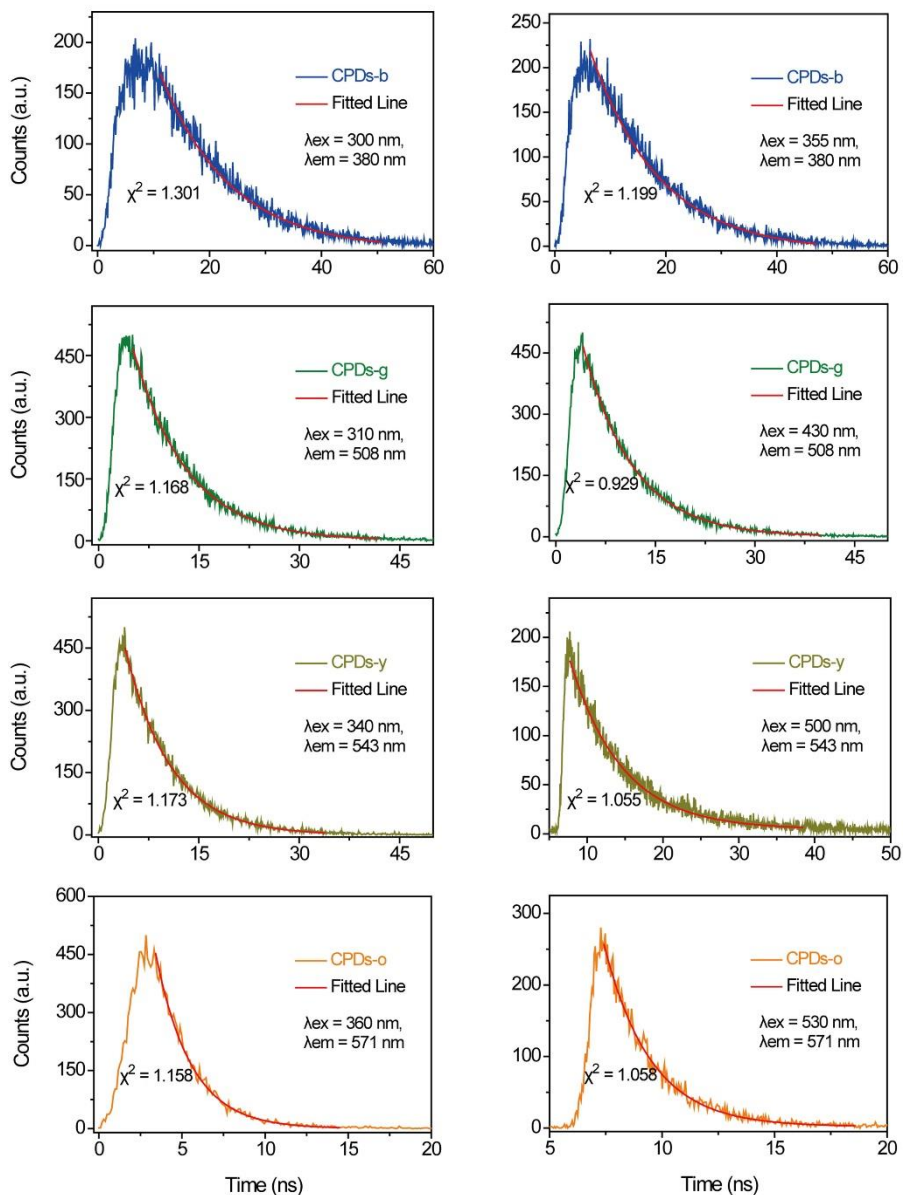
	λex [nm]	λem [nm]	B [%]	τ [ns]	χ^2
CPDs-b	300	380	100	12.4	1.301
	355	380	100	12.4	1.199
CPDs-g	310	508	100	8.1	1.168
	430	508	100	7.5	0.929
CPDs-y	340	543	100	6.8	1.173
	500	543	100	6.9	1.055
CPDs-o	360	571	100	2.1	1.158
	530	571	100	2.1	1.058

Figure S8 Fluorescent decay curves of CPDs-b, CPDs-g, CPDs-y, and CPDs-o, and their calculated lifetime values. Related to Figure 4
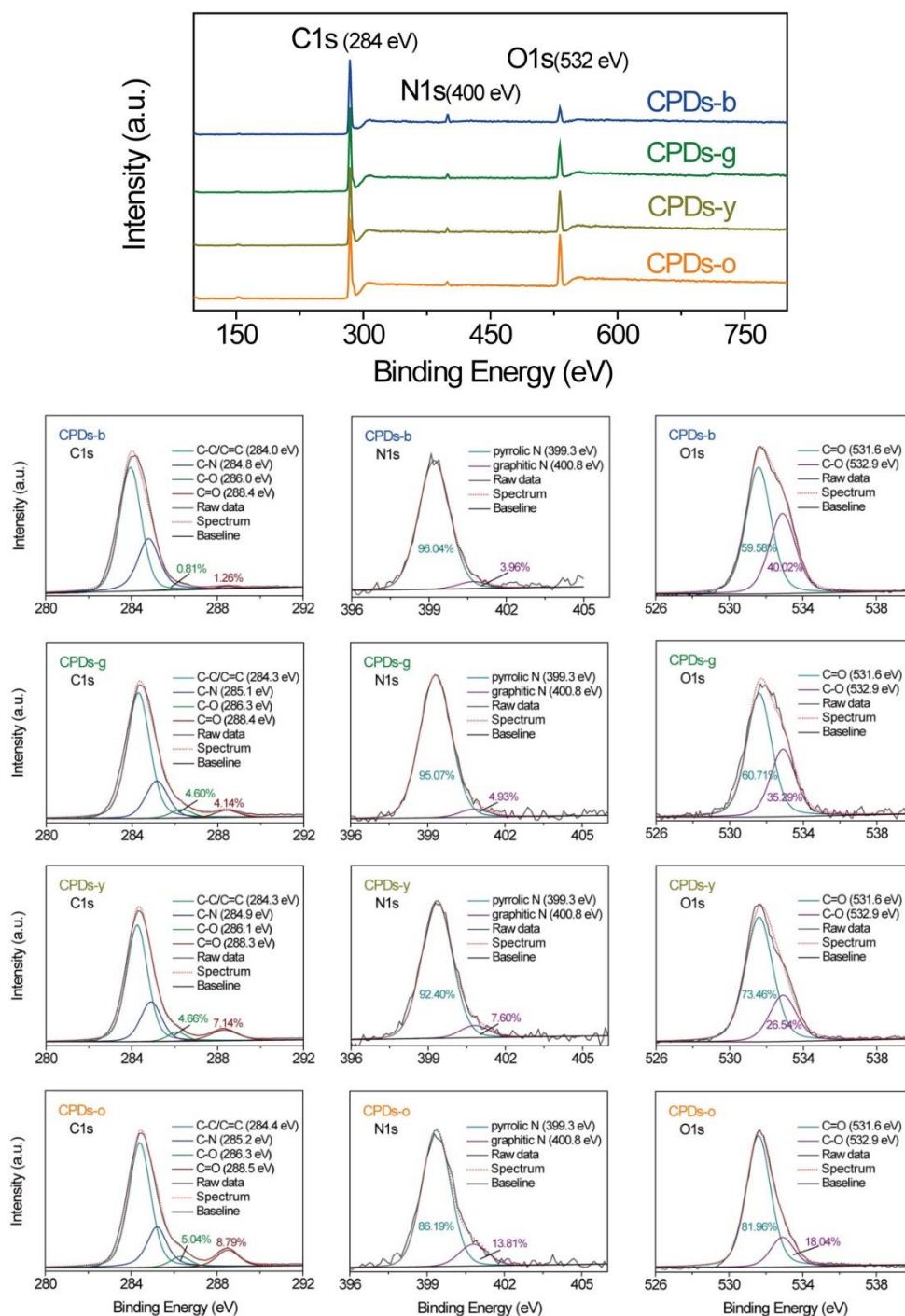
	C [%]	N [%]	O [%]	O/C
CPDs-b	87	4	9	0.09
CPDs-g	83	3	14	0.17
CPDs-y	81	3	16	0.20
CPDs-o	79	2	19	0.24

Figure S9 XPS spectra of CPDs-b, CPDs-g, CPDs-y, and CPDs-o, and each sample's element composition (obtained from XPS data). Related to Figure 5

a

b
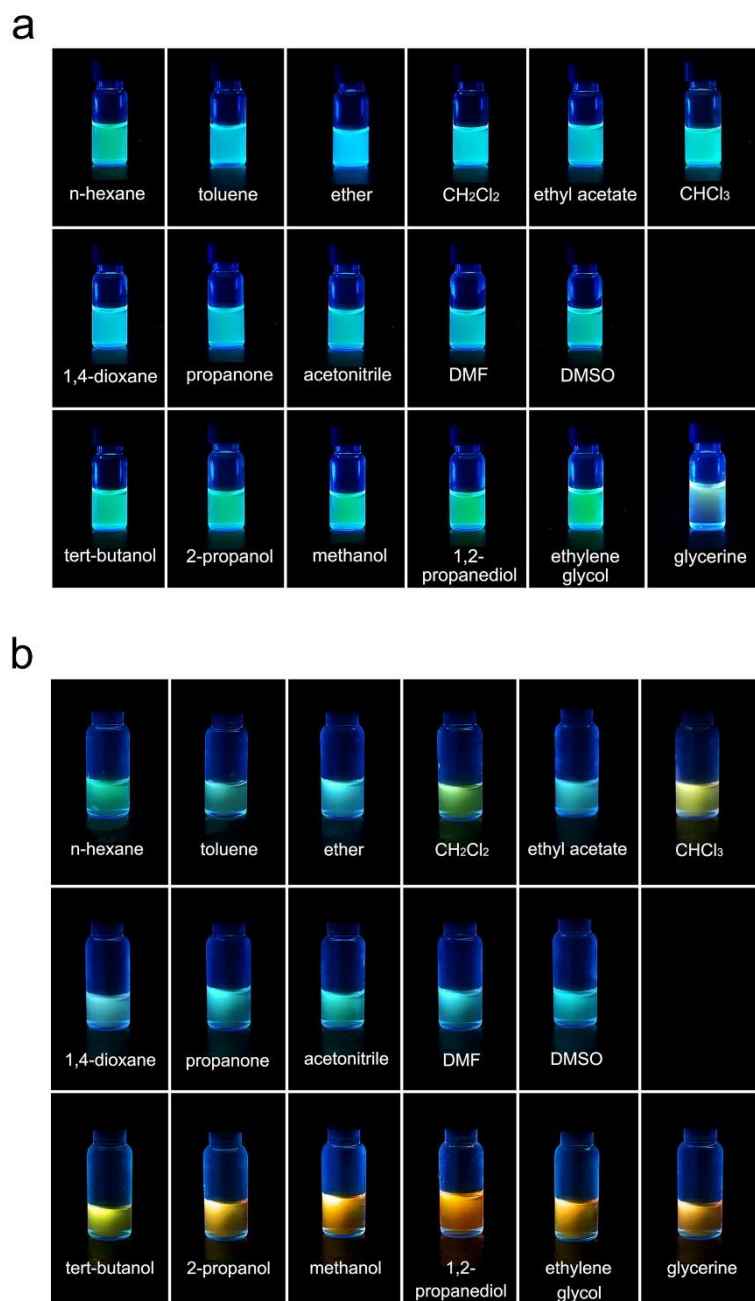
Figure S10 Photograph of CPDs-g **(a)** and CPDs-o **(b)** in different organic solvents (n-hexane, toluene, ether, dichloromethane, ethyl acetate, chloroform, 1,4-dioxane, propanone, acetonitrile, N,N-dimethylformamide, dimethyl sulfoxide, tert-butanol, 2-propanol, methanol, 1,2-propanediol, ethylene glycol, and glycerine) under 365 nm UV light excitation. Related to Figure 6
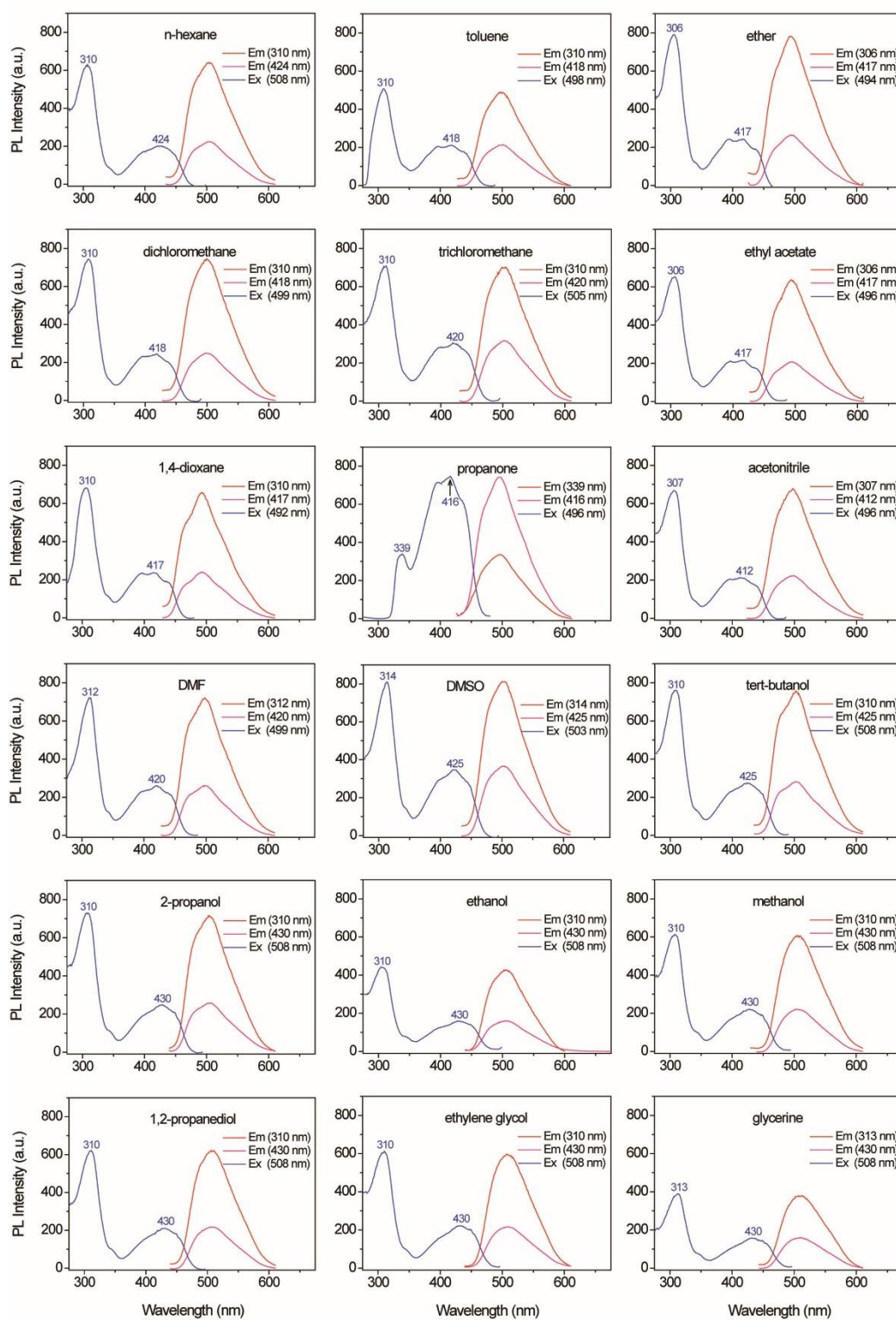
Figure S11 PL excitation (Ex) (red and pink lines), and emission (Em) (blue line) spectra of CPDs-g in different organic solvents (The same sequence with Figure S9a). Related to Figure 6

Note: Statistical data were listed in Table S5
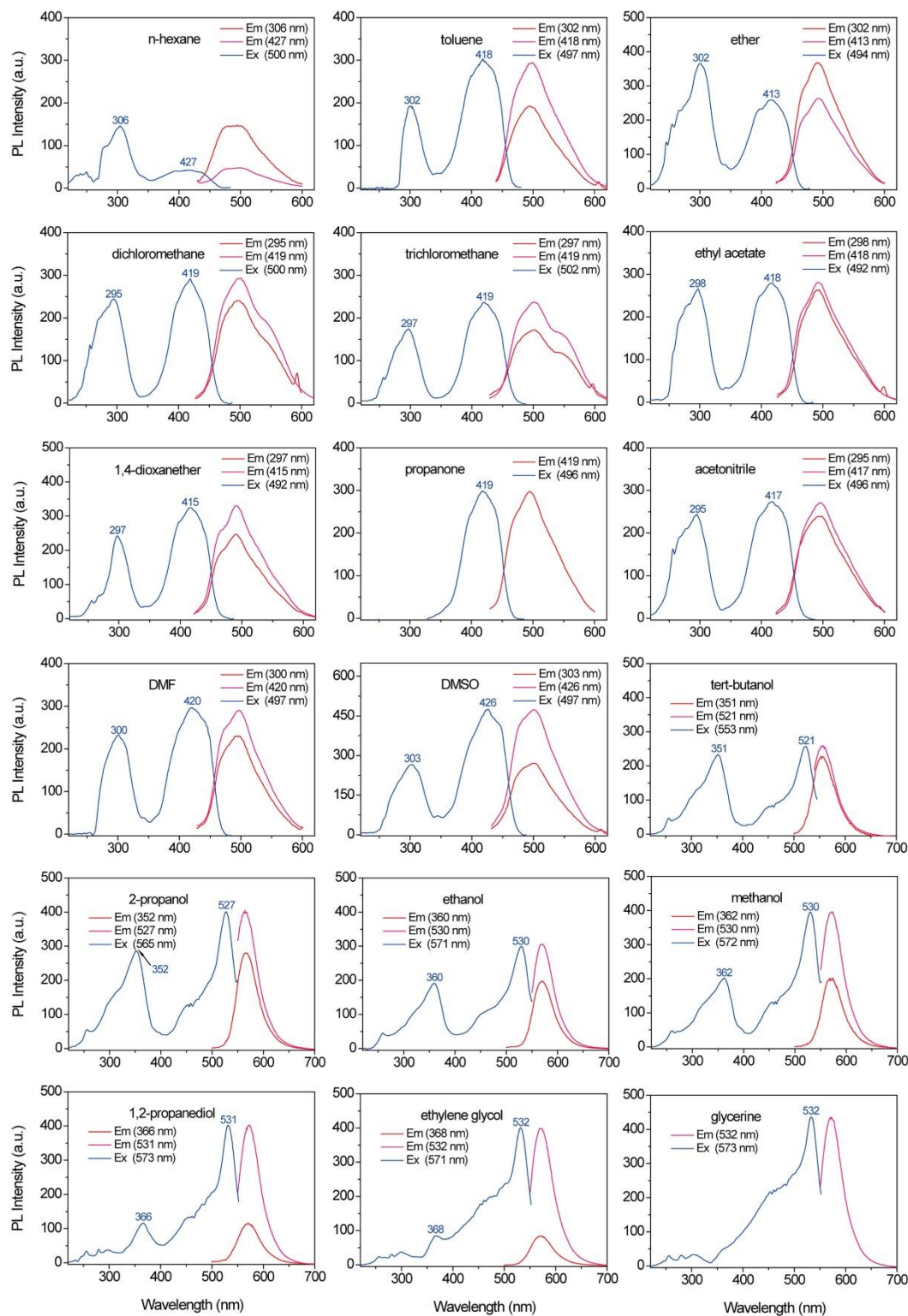
Figure S12 PL excitation (Ex) (red and pink lines), and emission (Em) (blue line) spectra of CPDs-o in different organic solvents (The same sequence with Figure S9b). Related to Figure 6

Note: Statistical data were listed in Table S6
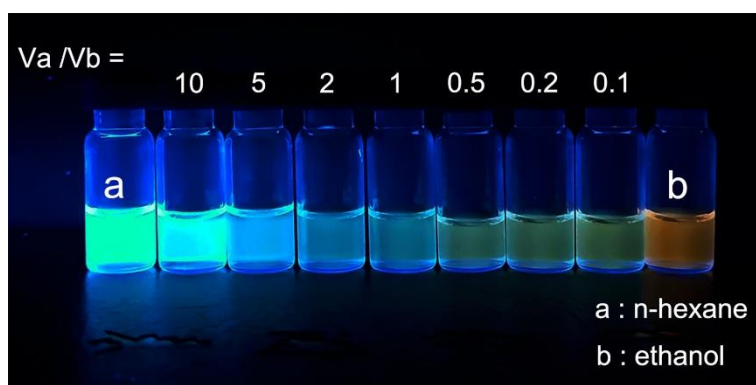
Figure S13 Photograph of CPDs-o in a mixed solution of n-hexane and ethanol with different volume ratios under 365 nm UV light excitation. Related to Figure 6
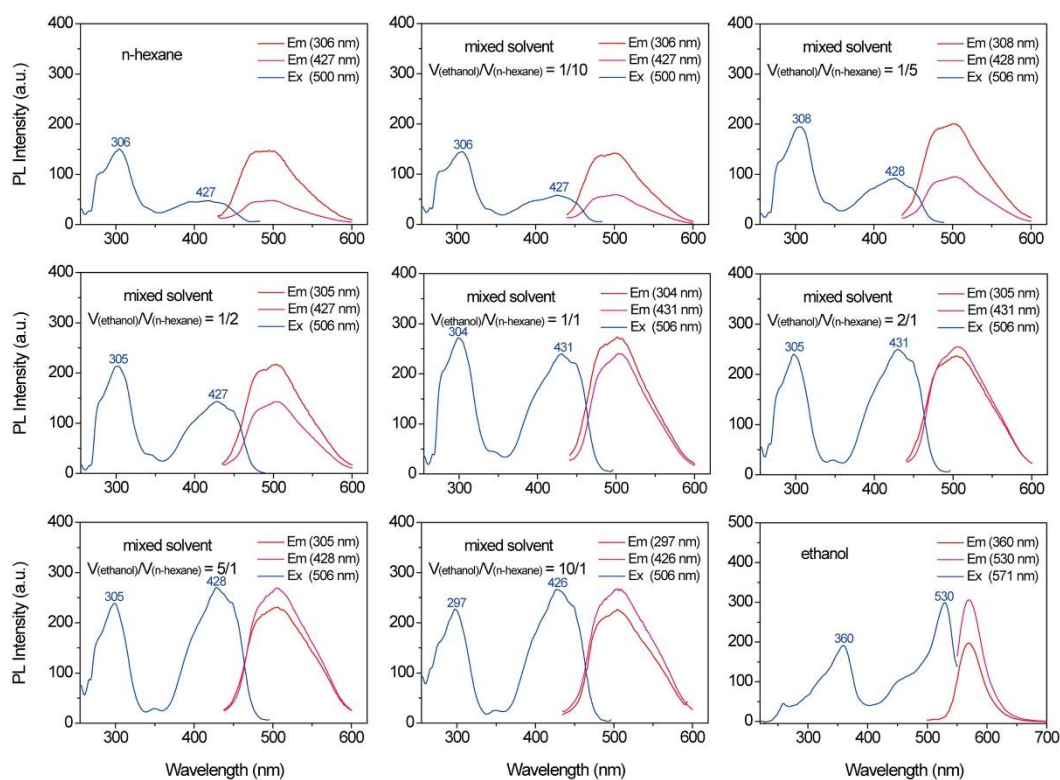
Figure S14 PL excitation (Ex) (red and pink lines), and emission (Em) (blue line) spectra of CPDs-o in mixed solutions of n-hexane and ethanol with different volume ratios. Related to Figure 6

Note: Statistical data were listed in Table S7
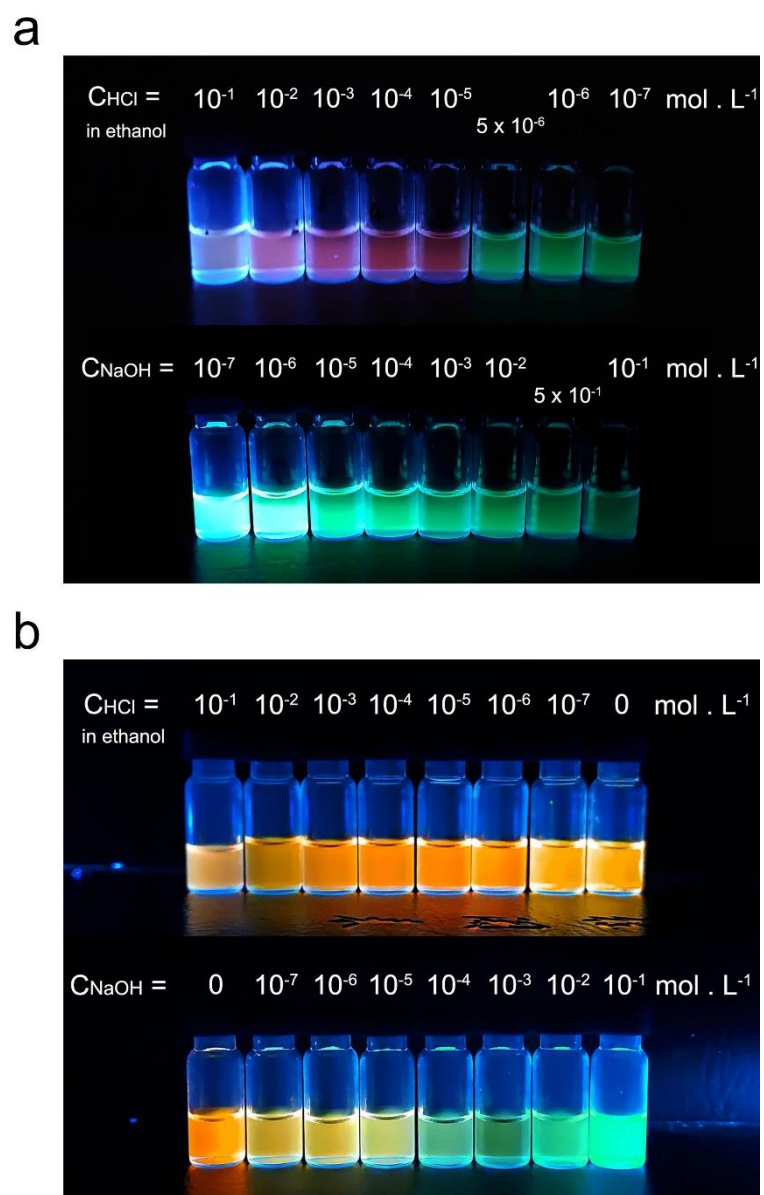
Figure S15 Photograph of CPDs-g **(a)** and CPDs-o **(b)** in acidic ethanol (HCl ethanol solution) and alkaline ethanol (NaOH ethanol solution) under 365 nm UV light excitation. Related to Figure 6
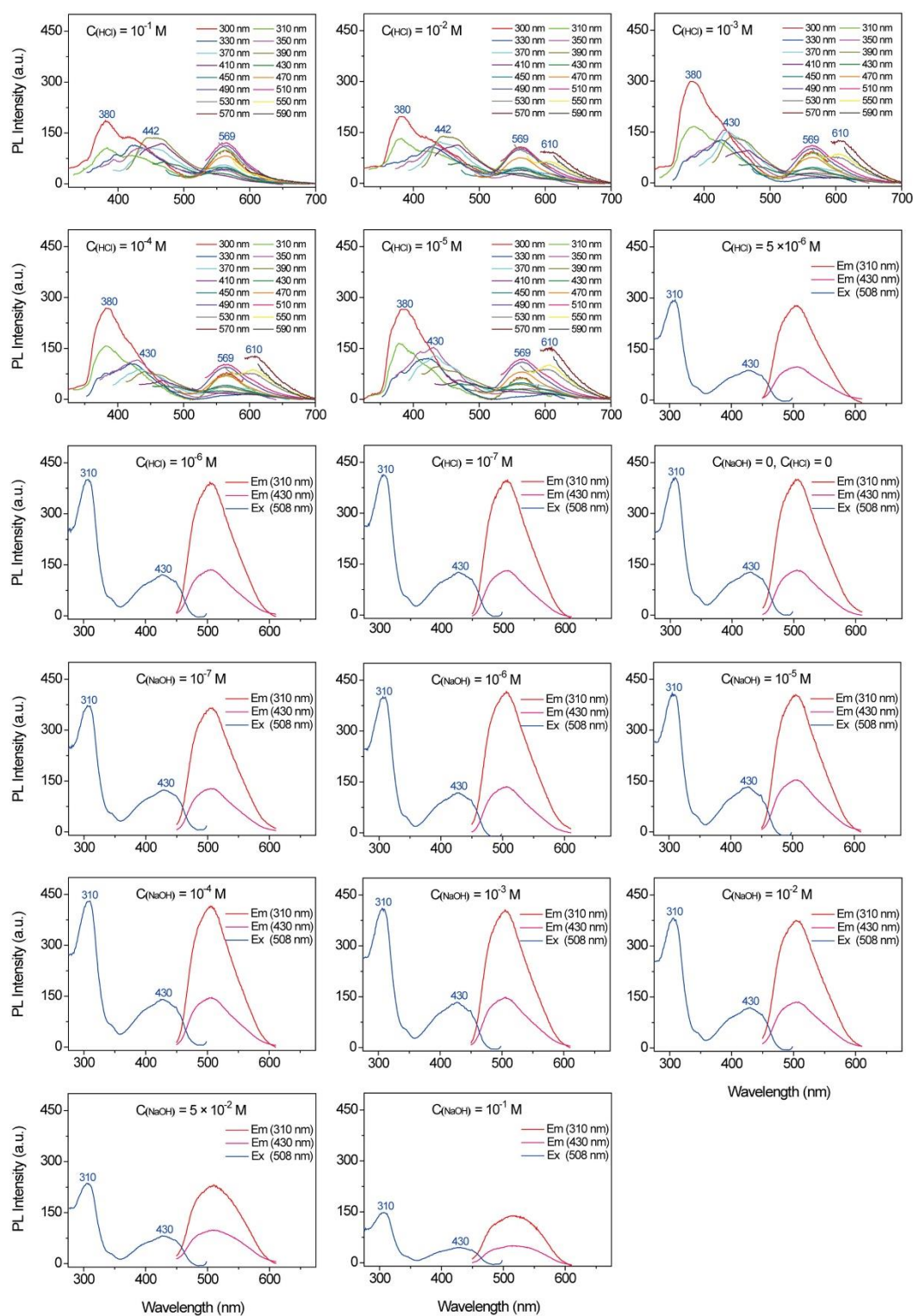
Figure S16 PL excitation (Ex) and emission (Em) spectra of CPDs-g in acidic ethanol with various HCl dosages, and alkaline ethanol with various NaOH dosages. Related to Figure 6

Note: Statistical data were listed in Table S8
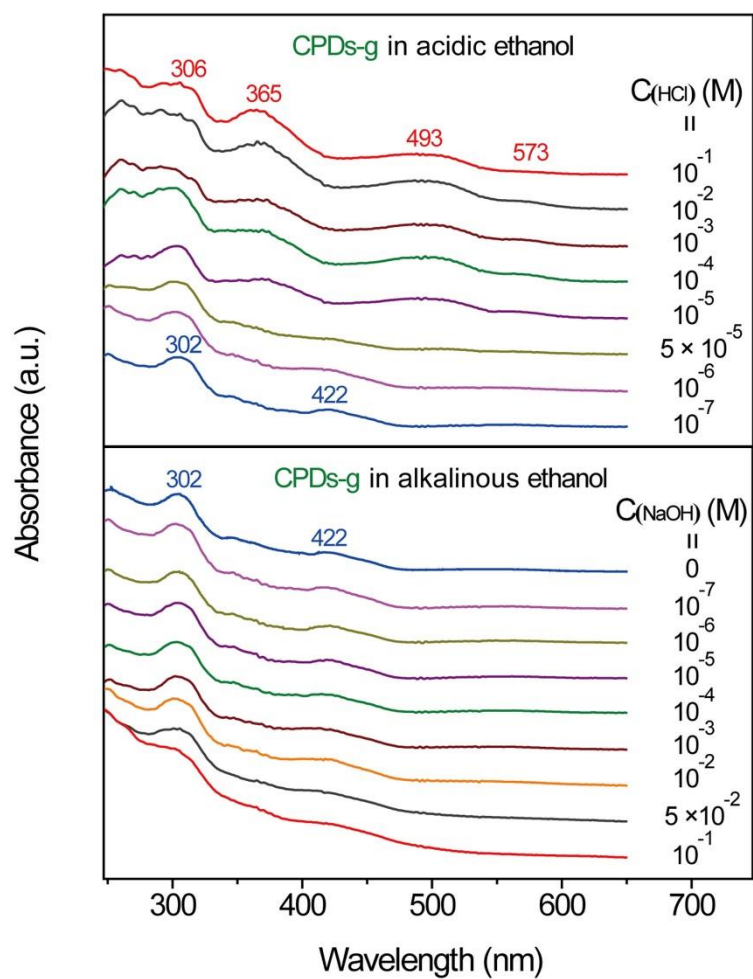
Figure S17 UV-Vis absorption spectra of CPDs-g in acidic ethanol with various HCl dosages, and alkaline ethanol with various NaOH dosages. Related to Figure 6

Figure S18 PL excitation (Ex) and emission (Em) spectra of CPDs-o in acidic ethanol with various HCl dosages, and alkaline ethanol with various NaOH dosages. Related to Figure 6

Note: Statistical data were listed in Table S9
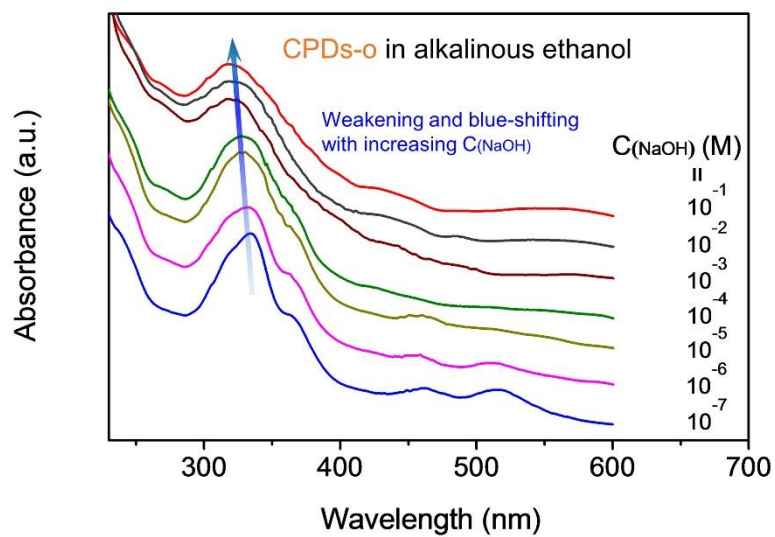
Figure S19 UV-Vis absorption spectra of CPDs-o in alkaline ethanol with various NaOH dosages (the relative absorption spectra of CPDs-o in acidic ethanol were shown in Figure 6). Related to Figure 6
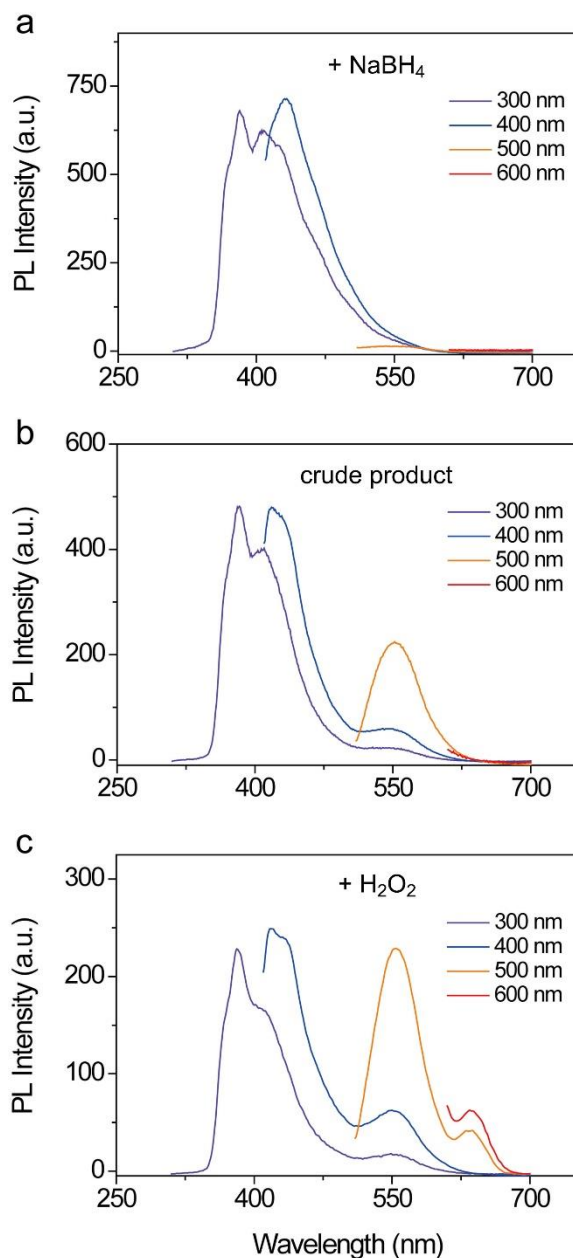
Figure S20 PL emission spectra with different excitation wavelengths of reaction crude product with adding of excess $NaBH_4$ or H_2O_2 (the crude solution was diluted tenfold by ethanol). **(a)** Crude product with adding of excess $NaBH_4$. **(b)** Crude product. **(c)** Crude product with adding of excess H_2O_2. Related to Figure 6
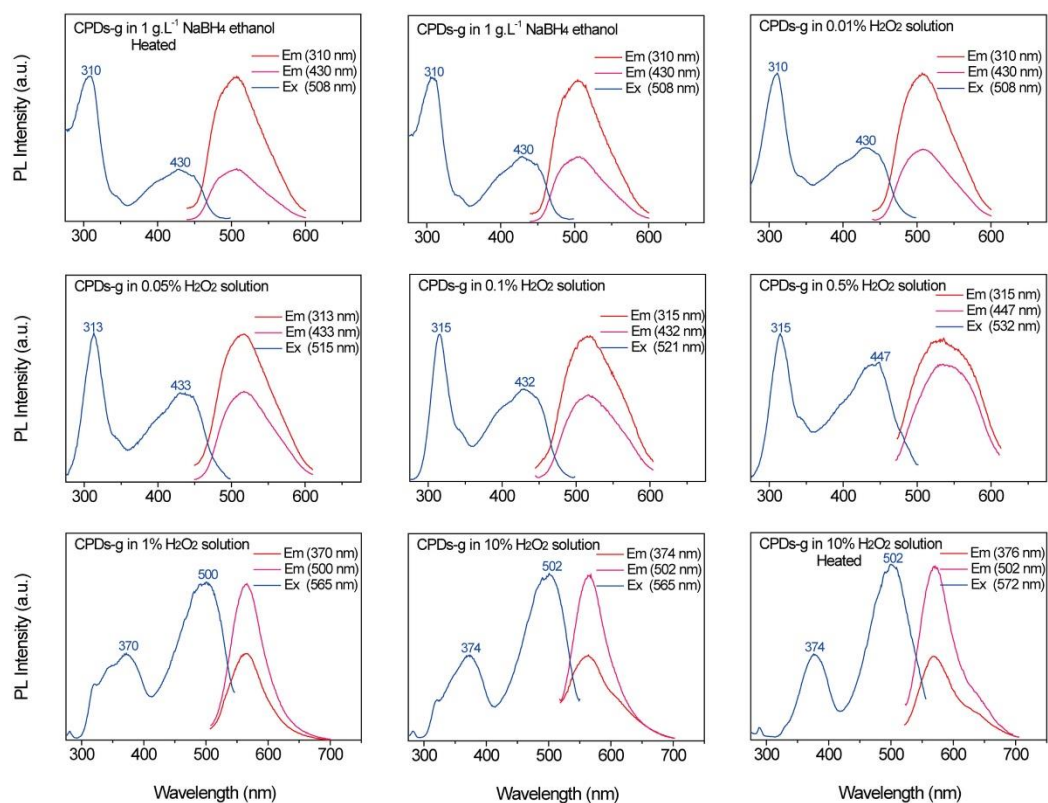
Figure S21 PL excitation (Ex) and emission (Em) spectra of CPDs-g in NaBH$_4$ or H$_2$O$_2$ solution. The first and last sample were CPDs-g NaBH$_4$ solution and CPDs-g H$_2$O$_2$ solution, respectively, which were kept at 60 °C for 12 h in an air oven. The other samples were CPDs-g H$_2$O$_2$ solution with different H$_2$O$_2$ dosages under room temperature. Related to Figure 6
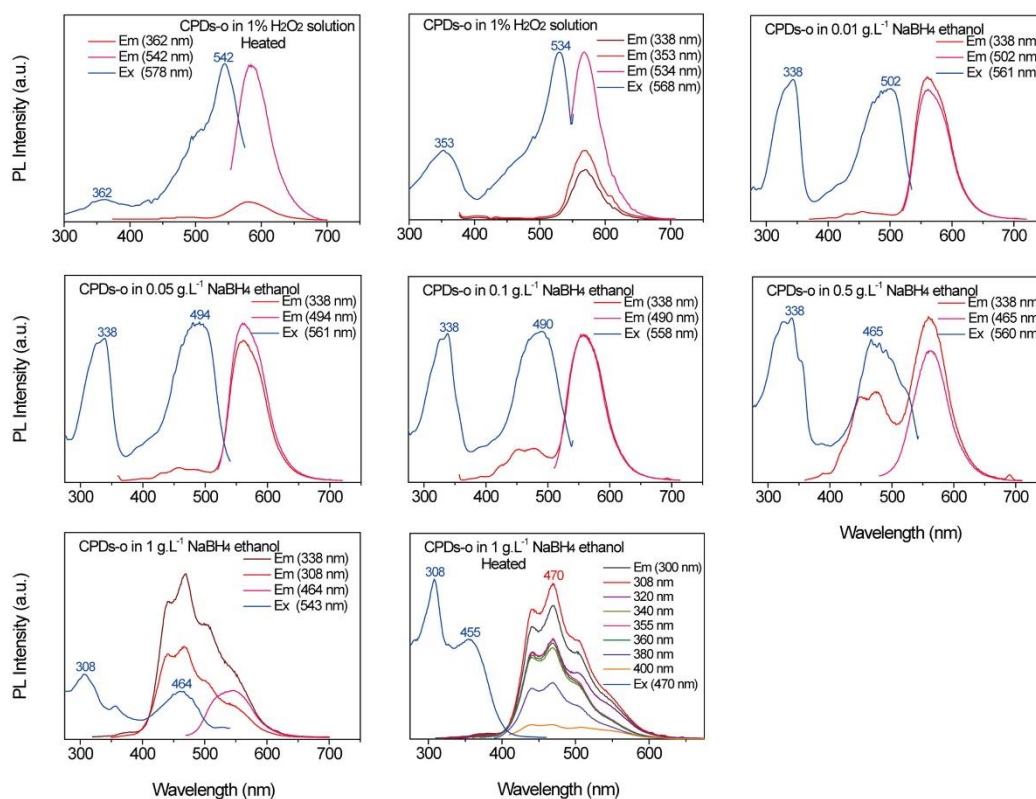
Figure S22 PL excitation (Ex) and emission (Em) spectra of CPDs-o in NaBH₄ or H₂O₂ solution. The first and last sample were CPDs-o H₂O₂ solution and CPDs-g NaBH₄ solution, respectively, which were kept at 60 °C for 12 h in an air oven. The other samples were CPDs-o NaBH₄ solution with different NaBH₄ dosages under room temperature. Related to Figure 6
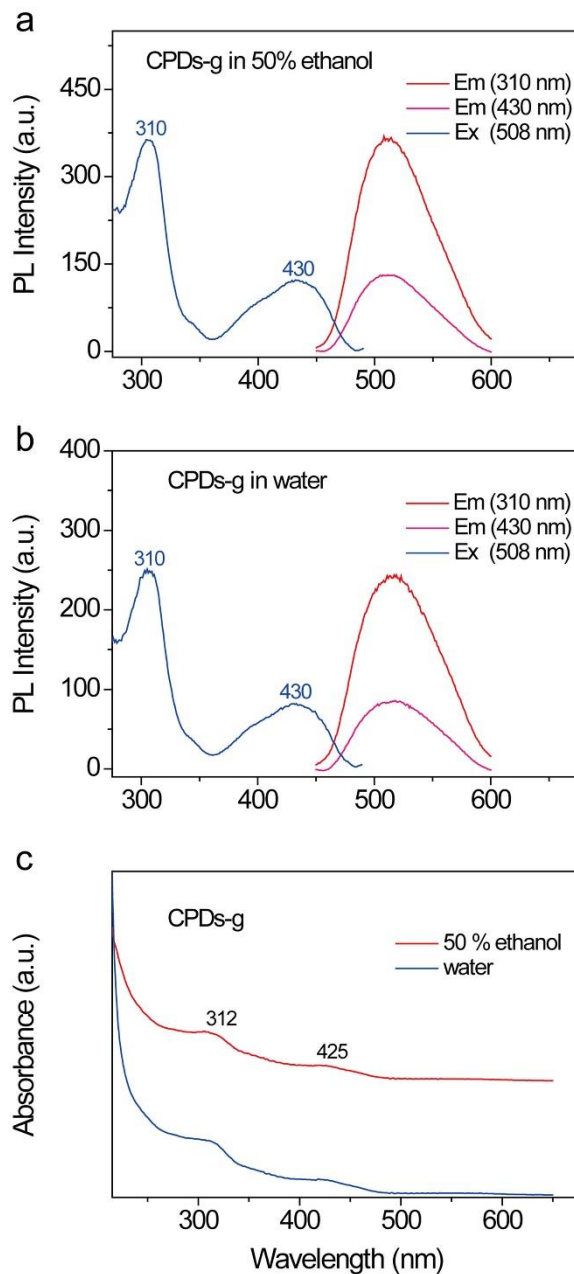
Figure S23 PL excitation (Ex) (red and pink lines), and emission (Em) (blue line) spectra of CPDs-g in 50% ethanol **(a)** and water **(b)**. **(c)** UV-Vis absorption spectra of CPDs-g in 50% ethanol and water. Related to Figure 6

Supplementary Tables:

Table S1 The influence of H_2O_2 dosage on the yield of CPDs with shorter-wave and longer-wave emission, and full-color fluorescent CPDs. Related to Figure 1

	0	0.08 mL	0.16 mL	0.32 mL	0.48 mL
CPDs-1 to -6	52% ± 2.5%	45% ± 2.5%	36% ± 2.0%	23% ± 4.2%	8% ± 2.6%
CPDs-7 to -10	-	6% ± 1.2%	12% ± 3.2%	18% ± 4.0%	5% ± 0.6%
CPDs-1 to -10	52% ± 2.5%	50% ± 3.5%	48% ± 1.5%	41% ± 1.7%	13% ± 3.1%

Table S2 The influence of HCl dosage on the yield of CPDs with shorter-wave and longer-wave emission, and full-color fluorescent CPDs. Related to Figure 1

	0	0.03 mL	0.06 mL	0.12 mL	0.24 mL
CPDs-1 to -6	4%± 1.5%	41% ± 2.9%	37% ± 1.5%	38% ± 2.3%	40% ± 3.5%
CPDs-7 to -10	-	10% ± 3.0%	12% ± 2.1%	10% ± 0.6%	11% ± 0.6%
CPDs-1 to -10	4%± 1.5%	51% ± 1.5%	48% ± 4.5%	49% ± 2.1%	51% ± 3.0%

Table S3 Basic optical data of CPDs-1 to -10. Related to Figure 3 and Figure 4

|	Abs-1 [nm]	Ex-1 [nm]	Abs-2 [nm]	Ex-2 [nm]	Em [nm]	Stokes shift-1 [nm]	Stokes shift-2 [nm]
CPDs-1	276	289	-	-	333	57	-
CPDs-2	282	300	330	354	380	98	50
CPDs-3	283	300	333	364	416	133	83
CPDs-4	293	305	368	373	437	144	69
CPDs-5	302	313	417	421	475	173	58
CPDs-6	302	311	422	431	508	206	86
CPDs-7	338	343	480	503	543	205	63
CPDs-8	350	360	506	529	571	221	65
CPDs-9	357	372	540	553	587	230	47
CPDs-10	372	384	565	581	608	236	43

The table corresponded to the Figure 3. (Abs-1: the first peak at UV-Vis absorption curve; Abs-2: the second peak at UV-Vis absorption curve; Ex-1: the first peak at PL excitation curve; Ex-2: the second peak at PL excitation; Stokes shift-1 = $\lambda_{Em} - \lambda_{Abs-1}$; Stokes shift-2 = $\lambda_{Em} - \lambda_{Abs-2}$).

Table S4 XPS data analyses of the C 1s, N 1s, and O 1s spectra of CPDs-b, CPDs-g, CPDs-y, and CPDs-o. Related to Figure 5

		CPD-b	CPDs-g	CPDs-y	CPDs-o
C1s	C−C/C=C	66%	71%	68%	64%
	C−N	32%	21%	21%	22%
	C−O	1%	5%	5%	5%
	C=O	1%	4%	7%	9%
N1s	pyrrolic N	96%	95%	92%	86%
	graphitic N	4%	5%	8%	14%
O1s	C=O	60%	61%	73%	82%
	C−O	40%	35%	27%	18%

Table S5 PL data of CPDs-g in different organic solvents. Related to Figure 6

CPDs-g	Solvent	Ex-1 [nm]	Ex-2 [nm]	Em [nm]	I_{Ex-1}/I_{Ex-2}
Non-alcoholic solvent	n-hexane	310	424	508	3.1
	toluene	310	418	498	2.4
	ether	306	417	494	3.1
	CH_2Cl_2	310	418	499	3.1
	ethyl acetate	306	417	496	3.1
	$CHCl_3$	310	420	505	2.4
	1,4-dioxane	310	417	492	3.0
	propanone	339	416	496	0.4
	acetonitrile	307	412	496	3.1
	DMF	312	420	499	2.9
	DMSO	314	425	503	2.4
Alcoholic solvent	tert-butanol	310	425	508	2.9
	2-propanol	310	430	503	2.9
	ethanol	310	430	508	2.9
	methanol	310	430	508	2.8
	1,2-propanediol	310	430	508	2.7
	ethylene glycol	310	430	508	2.6
	glycerine	313	430	508	2.4

The table corresponded to Figure S11

Table S6 PL data of CPDs-o in different organic solvents. Related to Figure 6

CPDs-o	Solvent	Ex-1 [nm]	Ex-2 [nm]	Em [nm]	I_{Ex-1}/I_{Ex-2}
Non-alcoholic solvent	n-hexane	306	427	500	3.3
	toluene	302	418	497	0.7
	ether	302	413	494	1.4
	CH_2Cl_2	295	419	500	0.4
	ethyl acetate	298	418	492	0.9
	$CHCl_3$	297	419	502	0.7
	1,4-dioxane	297	415	492	0.7
	propanone	-	419	496	-
	acetonitrile	295	417	496	0.8
	DMF	300	420	497	0.7
	DMSO	303	426	497	0.6
Alcoholic solvent	tert-butanol	351	521	553	0.9
	2-propanol	352	527	565	0.7
	ethanol	360	530	571	0.6
	methanol	362	530	572	0.5
	1,2-propanediol	366	531	573	0.3
	ethylene glycol	368	532	571	0.2
	glycerine	-	532	573	-

The table corresponded to the Figure S12. The Ex-1 peak of CPDs-o disappeared in propanone and glycerine solvents

Table S7 PL data of CPDs-o in a mixed solution of n-hexane and ethanol with different volume ratios. Related to Figure 6

No.	Mixed solvent	Ex-1 [nm]	Ex-2 [nm]	Em [nm]	I_{Ex-1}/I_{Ex-2}
1	n-hexane	306	427	500	3.3
2	Va/Vb = 10/1	306	427	500	2.6
3	5/1	308	428	506	2.2
4	2/1	305	427	506	1.5
5	1/1	304	431	506	1.1
6	1/2	305	431	506	1.0
7	1/5	305	428	506	0.9
8	1/10	297	426	506	0.8
9	ethanol	360	530	571	0.6

The table corresponded to Figure S14 (a: n-hexane, b: ethanol)

Table S8 PL data of CPDs-g in acidic or alkalinous ethanol. Related to Figure 6

$C_{(HCl)}$ [M]	Fluorescent property	Ex-1 [nm]	Ex-2 [nm]	Em [nm]	I_{Ex-1}/I_{Ex-2}
10^{-1}	excitation-dependent	-	-	380, 442, 569	-
10^{-2}	excitation-dependent	-	-	380, 442, 569, 610	-
10^{-3}	excitation-dependent	-	-	380, 430, 569, 610	-
10^{-4}	excitation-dependent	-	-	380, 442, 569, 610	-
10^{-5}	excitation-dependent	-	-	380, 442, 569, 610	-
5×10^{-6}	excitation-independent	310	430	508	3.2
10^{-6}	excitation-independent	310	430	508	3.3
10^{-7}	excitation-independent	310	430	508	3.2
0	excitation-independent	310	430	508	3.0
$C_{(NaOH)}$ [M]	Fluorescent property	Ex-1 [nm]	Ex-2 [nm]	Em [nm]	I_{Ex-1}/I_{Ex-2}
10^{-7}	excitation-independent	310	430	508	3.1
10^{-6}	excitation-independent	310	430	508	3.2
10^{-5}	excitation-independent	310	430	508	3.1
10^{-4}	excitation-independent	310	430	508	3.1
10^{-3}	excitation-independent	310	430	508	3.1
10^{-2}	excitation-independent	310	430	508	3.2
5×10^{-2}	excitation-independent	310	430	508	3.0
10^{-1}	excitation-independent	310	430	508	3.3

The table corresponded to Figure S16

Table S9 PL data of CPDs-o in acidic or alkalinous ethanol Related to Figure 6

$C_{(HCl)}$ [M]	Fluorescent property	Ex-1 [nm]	Ex-2 [nm]	Em [nm]	I_{Ex-1}/I_{Ex-2}
10^{-1}	excitation-independent	365	534	569	0.35
10^{-2}	excitation-independent	363	534	570	0.38
10^{-3}	excitation-independent	363	534	568	0.43
10^{-4}	excitation-independent	363	534	570	0.48
10^{-5}	excitation-independent	364	534	570	0.54
10^{-6}	excitation-independent	364	534	569	0.59
10^{-7}	excitation-independent	363	533	569	0.57
10^{-8}	excitation-independent	363	533	568	0.62
0	excitation-independent	360	530	571	0.64
$C_{(NaOH)}$ [M]	Fluorescent property	Ex-1 [nm]	Ex-2 [nm]	Em [nm]	I_{Ex-1}/I_{Ex-2}
10^{-7}	excitation-dependent	-	-	390, 508, 560	-
10^{-6}	excitation-dependent	-	-	390, 508, 563	-
10^{-5}	excitation-dependent	-	-	390, 508, 568	-
10^{-4}	excitation-dependent	-	-	390, 508, 570	-
10^{-3}	excitation-dependent	-	-	390, 508	-
10^{-2}	excitation-dependent	-	-	390, 515	-
10^{-1}	excitation-dependent	-	-	390, 515	-

The table corresponded to Figure S18

Transparent Methods

Materials.

Indole, indoline, seven methylindoles (1-methylindole, 2-methylindole, 3-methylindole, 4- methylindole, 5- methylindole, 6-methylindole, 7-methylindole), 30% H_2O_2, periodic acid, tert-butyl peroxide, and sodium borohydride were purchased from Aladdin Chemistry Co., Ltd. (Shanghai, China). Acid (38% HCl, HNO_3, CF_3COOH, CH_3COOH, H_3PO_4, and H_2SO_4), alkali (NaOH), and other organic solvents (n-hexane, toluene, ether, dichloromethane, ethyl acetate, chloroform, 1,4-dioxane, propanone, acetonitrile, N,N-dimethylformamide, dimethyl sulfoxide, tert-butanol, 2-propanol, methanol, ethanol, 1,2-propanediol, ethylene glycol, and glycerine) were obtained from Kelong Chemistry Co., Ltd. (Chengdu, China). All chemicals and solvents were directly used as received. Deionized water (di-water) was obtained from a Millipore system (Milli-Q).

Instruments and characterizations.

UV-Vis absorption spectra were recorded on a Shimadzu UV-2550 spectrometer. PL spectra were carried out with a Shimadzu RF-5301PC spectrofluorometer. The PL lifetimes and absolute quantum yields of the CPDs were measured by an Edinburgh Instruments FLS-980 Fluorescence Spectrometer. The size and morphologies of CPDs were measured by transmission electron microscope (TEM, JEM-2100, JEOL) and atomic force microscopy (AFM, Cypher ES, MicroDemo). The XRD data were investigated on a Shimadzu XRD-7000 diffractometer at 40 kV and 30 mA with Cu Kα radiation (λ = 0.15406 nm) in the 2θ range from 10º to 80º with 5º/min. Raman scattering spectra were obtained from a Horiba LabRAM HR Evolution Raman spectrometer with a laser of 785 nm wavelength using KBr as a dispersant and fluorescence quencher. The Fourier transform infrared (FT-IR) data were determined by a Thermo Scientific Nicolet 6700 FT-IR spectrometer. X-ray photoelectron spectroscopy (XPS) was performed on a Thermo Scientific ESCALAB 250Xi electron spectrometer. NMR measurements were taken by AVANCE III 400 (Bruker).

Tip. Instrument response function (IRF) of PL decay characterizations

		Manual measurement		TCC			
	λex [nm]	Source	Bandwidth [nm]	Start Rate [Hz]	Stop Rate [Hz]	Channel	Time [ch]
CPDs-b	300	nF920	19.00	40180	100	1024	0.09766
	355	nF920	19.00	40170	40	1024	0.09766
CPDs-g	310	nF920	10.00	40170	1390	1024	0.09766
	430	nF920	16.00	40170	1470	1024	0.09766
CPDs-y	340	nF920	19.00	40170	170	1024	0.09766
	500	TCSPC	3.00	2.00×10^7	1010	1024	0.04883
CPDs-o	360	nF920	19.00	40160	1530	1024	0.09766
	530	TCSPC	3.00	2.00×10^7	990	1024	0.04883

Synthesis and purification of full-color CPDs

0.4 g indole (3.4 mmol), 0.06 mL 38% HCl (0.74 mmol), and 0.16 mL 30% H_2O_2 (1.59 mmol) were dissolved into 10 mL ethanol with ultrasonic treatment, then the solution was transferred into a 20 mL Teflon reactor and maintained at 180 °C for 1.5 h in an air oven. To separate completely the components and build up orderly layers of fluorescent color, column chromatography and solid phase sample introduction were adopted. Firstly, the as-prepared dark red liquid was mixed with 1.2~2.0 g 200-mesh silica-gel powder, and then the excess solvent (including a part of HCl and H_2O_2) was removed by a rotary evaporator with reduced pressure. Subsequently, the dried powder was added into the column which was filled with the silica-gel powder soaked with eluent. When using the mixture of ethanol and ethyl acetate ($V_{ethanol}/V_{ethyl\ acetate}$ = 1/10) as an eluent, the CPDs showed an orderly distribution in the silica-gel column. Based on the dividing line of green and yellow fluorescence on the above silica-gel column, the CPDs could be easily divided into two parts, which were named as part A (containing CPDs-1 to -6) and part B (containing CPDs-7 to -10), respectively. The part B could be completely separated by using a mixture of ethanol and ethyl acetate ($V_{ethanol}/V_{ethyl\ acetate}$ = 1/5 to 1/2), while the part A needed an eluent with lower polarity, such as a mixture of ethyl acetate and dichloromethane ($V_{dichloromethane}/V_{ethyl\ acetate}$ = 1/10 to 1/1). Finally, the obtained ten CPD samples with different fluorescence were redispersed in ethanol solutions.

Synthesis of CPDs from other reagents

(1) Similarly to the synthesis process of indole-based full-color CPDs, 0.4 g indoline (3.4 mmol) or 0.45 g methylindole (3.4 mmol), 0.06 mL 38% HCl (0.74 mmol), and 0.16 mL 30% H_2O_2 (1.59 mmol) were used to prepare experimentally CPDs, which are shown in Figure 1d.

(2) 0.4 g indole (3.4 mmol), 0.06 mL 38% HCl (0.74 mmol), and 0.29 g tert-butyl peroxide (2.0 mmol) or 0.23g periodic acid (1.0 mmol) can also be used to prepare indole-based full-color CPDs, which are showed in Supplementary Figure 3.

(3) HCl (0.74 mmol) were equivalently replaced with H_2SO_4, H_3PO_4, CF_3COOH, HNO_3, and CH_3COOH, and the results are shown in the manuscript.

The speculations were provided, as follows:

(1) H_2O_2 and a few weak acids, such as CH_3COOH and $HCOOH$, lead to the scarce formation of CPDs with short-wave emission, and this may be due to the lack of enough H^+ to initiate polymerization.

(2) Periodic acid (HIO_4) can provide O_2 and H^+, so it can be used independently. In a published paper (Wang et al., 2017), KIO_4 was used as a unique oxidant, because it's product (namely, K^+ and IO_3^-) cannot affect the properties of the CPDs. Incidentally, $H^+ + KIO_4$ could also be used to produce multicolor fluorescent CPDs in this study.

(3) Some oxidative acids or $H^+ +$ oxidative salts, such as $KMnO_4$, $K_2Cr_2O_7$, lead to the formation of metal-containing byproducts which inhibit fluorescent emission. When using these additives only a black liquid without fluorescence is obtained.

(4) HNO_3 seem to be directly used both as an acid and an oxidative reagent, or just as an acid (with H_2O_2). However, extremely few CPDs with multicolor emission can be gained by using $HNO_3 + H_2O_2$, while CPDs with weak blue-green-yellow emission will be obtained by directly using HNO_3. Additionally, some indole substitutes (such as indole-6-carboxylic acid, 6-fluoroindole, 6-nitroindole, 6-hydroxyindole, and so on) were treated under optimal conditions to study the effect of substituents on the fluorescence of CPDs. It can be found that the

passivation groups (such as -NO$_2$) on the benzene ring may inhibit cationic polymerization and oxidation, and thus decrease the formation of ideal CPDs. Considering these phenomena, it can be assumed that HNO$_3$ tends to react with indole to generate nitroindole at the beginning of the reaction, which inhibits the formation of multicolor fluorescent CPDs.

Supplemental References

Wang, Z., Yuan, F., Li, X., Li, Y., Zhong, H., Fan, L., and Yang, S. (2017). 53% efficient red emissive carbon quantum dots for high color rendering and stable warm white-light-emitting diodes. Adv. Mater. *29*, 1702910